Assessment of Hybrid CFD Turbulence Model, STRUCT-ε, for Thermal Striping Behavior

by

Brendan Conor Vaughan

S.B. Nuclear Science and Engineering
Massachusetts Institute of Technology, 2023

Submitted to the Department of Nuclear Science and Engineering
in partial fulfillment of the requirements for the degree of

MASTER OF SCIENCE IN
NUCLEAR SCIENCE AND ENGINEERING

at the

MASSACHUSETTS INSTITUTE OF TECHNOLOGY

February 2024

Authored by: Brendan Conor Vaughan
Department of Nuclear Science and Engineering
January 19, 2024

Certified by: Emilio Baglietto
Department of Nuclear Science and Engineering
Associate Head, Department of Nuclear Science and Engineering
Thesis Supervisor

Accepted by: Ju Li
Department of Nuclear Science and Engineering
Chair, Department Committee on Graduate Students

Assessment of Hybrid CFD Turbulence Model, STRUCT-ε, for Thermal Striping Behavior

by

Brendan Conor Vaughan

Submitted to the Department of Nuclear Science and Engineering
on January 19, 2024, in partial fulfillment of the requirements for
the degree of
MASTER OF SCIENCE IN
NUCLEAR SCIENCE AND ENGINEERING

Abstract

Many advanced nuclear reactor designs are susceptible to thermal fatigue damage caused by thermal striping, which presently accepted modeling and design tools are unable to accurately or reliably predict. Advanced reactors are vital in achieving net-zero carbon electricity production and thus developing design tools that can predict thermal striping is essential. Any new design tool used in the nuclear industry must be validated against experimental data sets to ensure that results predicted by these methods are sufficiently accurate. The STRUCT-ε Computational Fluid Dynamics model was used to aid the development of a dedicated thermal striping experiment that will later be used to help validate the capabilities of various models.

The STRUCT-ε model provided the ability to conduct turbulence resolving simulations at a speed conducive to rapid iteration of the design of the DESTROJER test facility. To further increase confidence in the model's applicability to the test cases, two LES runs were completed and demonstrate the ability to capture flow unsteadiness with a Computation Fluid Dynamic model. However, in both test cases the STRUCT-ε model exaggerates the behavior seen in the LES runs; over predicting temperature oscillations in one case and the flow asymmetry in the other. The STRUCT-ε model's potential to predict asymmetric configurations provides promising further applications of the model. Future studies of STRUCT-ε should seek to better understand the model's performance in asymmetric flow cases to further support experimental design and the assessment of complex operating configurations.

Thesis Supervisor: Emilio Baglietto
Title: Department of Nuclear Science and Engineering
Associate Head, Department of Nuclear Science and Engineering

Acknowledgements

I want to first thank my research advisor, Professor Emilio Baglietto, for all of the help and guidance he has provided me during my time at MIT and for welcoming me like a member of his own family.

I would like to express my deepest gratitude to Heather Barry for all the amazing work she has done for me and other students to make the nuclear department a true community. She has helped me through a lot and I'm sure she will continue to help countless others.

I would also like to thank my friends and family for all of the support they have given me along the way. Thank you to my research group members who were always willing to help me work through roadblocks and for not attacking me as I hogged cluster nodes. Thank you to my friends who made my time between research so much fun and gave me plenty of memories to look back on fondly. Thank you to my family for all the love, affection, and effort that you poured into me to help me get where I have today. And thank you to everyone who helped me adapt to life as I entered active duty.

Finally, thank you to the U.S. Department of Energy Integrated Research Project "Center of Excellence for Thermal-Fluids Applications in Nuclear Energy: Establishing the knowledgebase for thermal-hydraulic multiscale simulation to accelerate the deployment of advanced reactors" - IRP-NEAMS-1.1: Thermal-Fluids Applications in Nuclear Energy who funded this work and who it would not have been possible to achieve without.

Contents

List of Figures

List of Tables

Chapter 1

Introduction

1.1 Motivation

The development and construction of nuclear power plants is necessary for the smooth transition to a decarbonized energy grid and to limit global temperature rise to below 2 ℃ [1][2]. The reactor designs being pursued for this transition are Generation IV reactors which aim to use fuel more efficiently, reduce waste production, be economically competitive, achieve higher safety standards, and be more proliferation resistant [3]. These Gen IV reactors utilize coolants, such as He gas, liquid sodium, and molten salts, that enable higher power plant performance. However, to operate these reactors effectively a thorough understanding of the coolant's behavior is vital. Coolant behavior fundamentally influences the neutronics, heat management, and control of radionuclides in the reactor.

Nuclear reactors that currently utilize non-water coolants represent only 3.2% of all active nuclear power plants, limiting operational and simulational experience with the coolant's behavior [4]. Of particular interest is thermal striping, a turbulence driven phenomena where coolant flows at different temperatures mix together in an oscillatory manner. These temperature oscillations can cause the temperature experienced by reactor components to oscillate in kind and cause thermal fatigue damage, decreasing the safety and reliability of the reactor [5]. Water-cooled nuclear reactors are currently evaluated using lumped parameter codes based on 1-dimensional

simplifications and are widely recognized and accepted for safety analysis by many nuclear regulatory bodies. However, because lumped parameter codes are based on 1-dimensional simplifications, they are unable to accurately predict thermal striping which is defined by its 3-dimensional and unsteady nature [6]. Water cooled reactor designs have higher material failure margins that allowed this inaccuracy to not be a concern, but non water cooled reactor designs rely on narrower margins due to their higher operating temperatures. To ensure that these reactors will operate continuously, more accurate methods that leverage smaller simulation errors are required to confirm that the material failure limits are respected.

Computational Fluid Dynamics (CFD) models have been explored as a more accurate alternative, but currently adopted industrial CFD models are not yet fully capable of tackling these phenomena with sufficient robustness. The assumptions and simplifications that allow the models to be computationally affordable cause the models to struggle to accurately predict the temperature profiles within reactor components [7]. Currently recognized CFD models either need large amounts of computing power in order to produce accurate results, making them impractical to use as a design tool, or are unable to resolve unsteady turbulent structures that lead to component failure in thermal striping [8]. The STRUCT-ε model, a so called "hybrid model", was specifically designed for unsteady turbulent flow mixing and compared to other models has been shown to be 70 times more computationally affordable while maintaining reliability [7]. STRUCT-ε thus offers the ability to quickly test a large number of test cases. However, the validation database used must be expanded in order to ensure its proper use in the licensing and design of advanced nuclear reactors [7].

The STRUCT-ε model will be used to perform a rapid design analysis of the DESTROJER test facility at the University of Michigan. In order to gauge the ability of the model to support a rapid design analysis, the model is assessed against Large Eddy Simulation (LES) results. The DESTROJER test facility will then be used to produce experimental results that will be utilized in the evaluation of CFD models as validation is most effective when experimental design is informed by a priori CFD

analysis [9]. If the STRUCT-ε model can be validated for use in predicting thermal striping then it can provide a sound basis for the design and material selection of reactor components and thus improve the viability of Generation IV reactor designs.

1.2 Previous Work

Previous work on the validation of STRUCT-ε was conducted using experimental data on impinging jet flow from the European Research Community on Flow, Turbulence, and Combustion [10]. Additional validation work was carried out using experimental data on the interaction of symmetric jets from the University of Michigan's Reactor Cavity Cooling System (RCCS) test facility [11]. However, the primary focus of the DESTROJER test facility is to investigate the flow behavior of two symmetric jets that are impinging upon a surface. The combination of jet mixing and impingement has the greatest potential to induce thermal striping and component damage in Generation IV reactors such as Terrapower's Natrium reactor or General Atomics's (GA) helium-cooled Fast Modular Reactor (FMR) [12]. This research project uses CFD simulation tools to assist in the validation and acceptance of STRUCT-ε as a safety analysis tool for nuclear reactor design, and is a continuation of the work initiated by Vaughan (2023) [13].

1.3 Objectives

The objective of this research project is to provide guidance on the design and selection of test cases for the DESTROJER test facility while advancing the validation of the STRUCT-ε model. This work will be accomplished by attempting to simulate and predict the temperature variance on the impinging plate across a range of potential test cases. The simulations will be done by varying the height of the impinging plate and the use of flow impeding obstacles.

To accomplish this goal, the author first learned the theory and use of CFD software. The software used was STAR-CCM+ version 16.04.012 from Siemens. Once

the author was proficient with the use of the software, work began on the use of the STRUCT-ε and LES model to simulate the DESTROJER test facility.

1.4 Structure

Chapter 1 provides an overview of the research project including goals and relevance.

Chapter 2 contains the background necessary to understand the DESTROJER test facility, the advantages and disadvantages of different classifications of CFD models, and the structure of the STRUCT-ε model.

Chapter 3 gives details of the methodology used to perform and analyze the CFD modeling for each test case.

Chapter 4 displays the results and evaluation of STRUCT-ε simulations for different impingement plate configurations of the DESTROJER test facility. Qualitative and quantitative analysis is performed to determine the experimental setup that is most likely to produce the thermal striping phenomena of interest.

Chapter 5 displays the results and evaluation of STRUCT-ε and LES simulations with a cylindrical obstacle intended to induce jet flow oscillations in the DESTROJER test facility. Qualitative and quantitative analysis is performed to determine if the use of an impeding obstacle in the experimental setup will aid in the production of the thermal striping phenomena of interest. The STRUCT-ε and LES model results are compared to assess the validity of the STRUCT-ε model.

Chapter 6 concludes the thesis and presents proposed future work.

Chapter 2

Background

2.1 DESTROJER Test Facility

Experiments at the University of Michigan will provide the ability to create relevant data sets for use in validation of the STRUCT-ε CFD model. The primary focus of the DESTROJER facility is to investigate the behavior of buoyant jets in a stratified environment [7]. The facility consists of a square prismatic gaseous fluid domain, two inlet jets, and an adjustable impingement plate. The DESTROJER test facility is illustrated in Figure 2.1.

Temperature data is collected at the bottom of the impingement plate by thermocouples (TCs) and a fiber optic sensor. The layout of the TCs and fiber optic sensor can be seen in Figure 2.2. For all simulations presented in this work, TCs are numbered starting at 1 above the hot jet and continue upwards to 32 above the cold jet. The TCs are quite fragile due to their small size; the TCs that have remained functional are shown colored in red and blue. The TCs used have a thermal response frequency of 68 Hz while the fiber optic sensor used has an estimated thermal response frequency of 62.5 Hz.

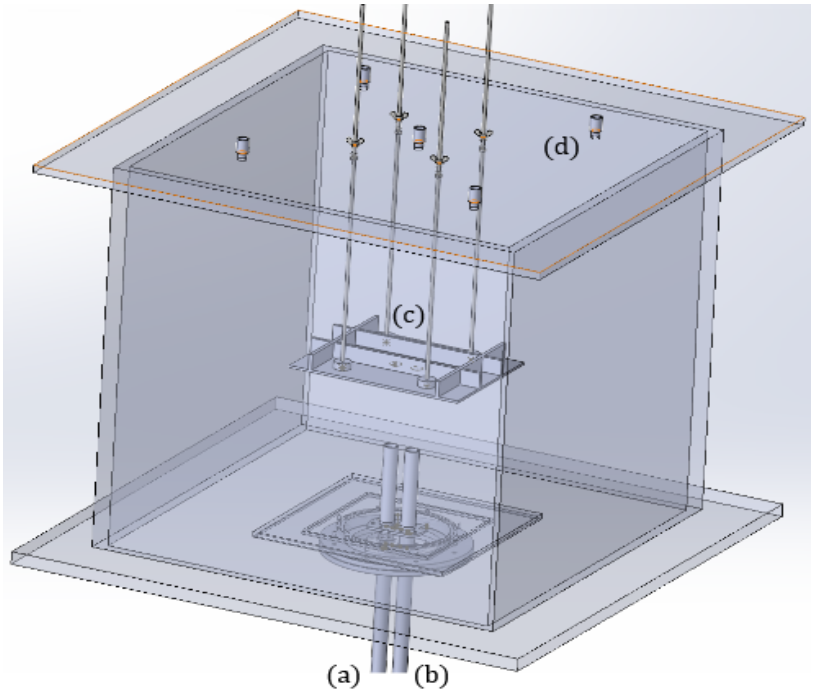

Figure 2.1: A view of the DESTROJER test facility geometry fluid domain showing the (a) hot inlet, (b) cold inlet, (c) impingement plate, and (d) the outlet valves, with one located in each corner. The central valve is used only for set up and is closed during experiment execution.

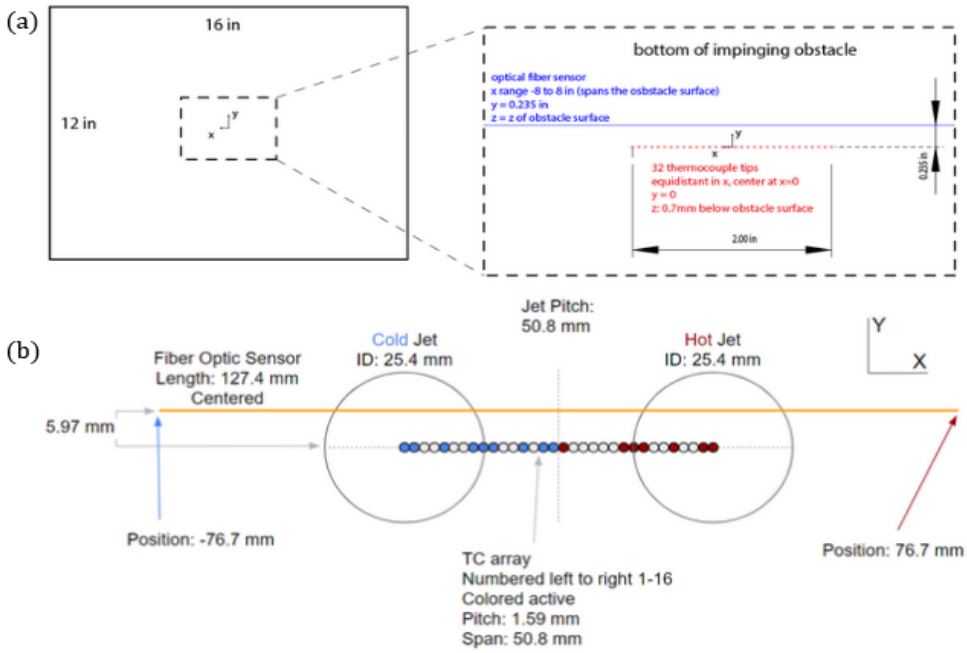

Figure 2.2: Schematic of the impingement plate showing a downward view of (a) the impingement plate dimensions with the locations of the fiber optic and TCs and (b) details of the fiber optic and TC placement projected onto a cross section of the jets.

2.2 Computational Fluid Dynamics

CFD is a numerical solution method that utilizes the discretized Navier-Stokes equations to calculate the behavior and quantities of physical significance for a particular fluid flow [14]. CFD is an invaluable tool for understanding fluid flows as it is able to provide data about a particular flow that cannot be captured in an experiment.

To accurately capture the values of these quantities of physical significance, the solution domain is divided into subdomains using a spatial grid. These subdomains are called cells. Within each of these cells, the Navier-Stokes equation are solved while ensuring the conservation of mass, momentum, and energy across the solution domain. The conservative differential form of the Navier-Stokes equations are as follows:

Mass:

$$\frac{\partial \rho}{\partial t} + \nabla \cdot \left(\rho \vec{U}\right) = 0 \tag{2.1}$$

Momentum:

$$\frac{\partial \left(\rho u\right)}{\partial t} + \nabla \cdot \left(\rho u \vec{U}\right) = -\frac{\partial P}{\partial x} + \nabla \cdot \left(\mu \nabla u\right) + S_{Mx} \tag{2.2}$$

$$\frac{\partial \left(\rho v\right)}{\partial t} + \nabla \cdot \left(\rho v \vec{U}\right) = -\frac{\partial P}{\partial y} + \nabla \cdot \left(\mu \nabla v\right) + S_{My} \tag{2.3}$$

$$\frac{\partial \left(\rho w\right)}{\partial t} + \nabla \cdot \left(\rho w \vec{U}\right) = -\frac{\partial P}{\partial z} + \nabla \cdot \left(\mu \nabla w\right) + S_{Mz} \tag{2.4}$$

Energy:

$$\frac{\partial \left(\rho c_p T\right)}{\partial t} + \nabla \cdot \left(\rho c_p T \vec{U}\right) = -P \nabla \cdot \vec{U} + \nabla \cdot \left(k \nabla T\right) + \phi + S_i \tag{2.5}$$

where u, v, and w are the x, y, and z velocities respectively of the velocity $\vec{U}$ [14]. This work will utilize the Finite Volume (FV) discretization, as it is the most widely used discretization method in CFD codes.

2.3 Turbulence

Turbulence is the irregular motion of a fluid that causes the velocity to fluctuate and the increased diffusion of conserved quanitites such as temperature [14]. Turbulent

flows are composed of rotating vortex structures known as eddies. The amount of turbulence in a flow can be predicted with the Reynolds Number,

$$Re = \frac{uL}{\nu} \tag{2.6}$$

where u is the bulk fluid velocity, L is the characteristic length scale, and ν is the kinematic viscosity [15].

The complexity of turbulent flows has made accurate numerical modelling difficult. Much of this complexity comes from the large range of length scales that define the eddies that make up the turbulent flow. The range of length scales that define turbulent flows are categorized using three primary length scales: the Kolmogorov scale, the Taylor microscale, and the integral scale as seen in Figure 2.3 [15].

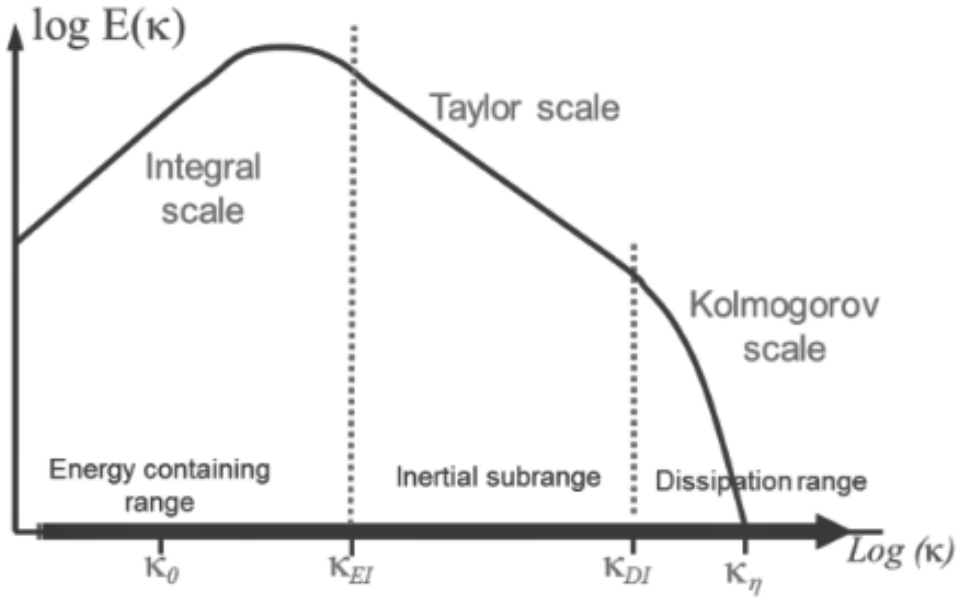

Figure 2.3: The Kolmogorov energy spectrum displaying the the relationship between the amount of turbulent energy contained within eddies of wavelength λ versus wave number κ where $\kappa = 2\pi/\lambda$ [16].

Most of the energy is carried by larger scale eddies whose length scale is determined by the geometry of the fluid domain. These larger eddies decay into smaller structures which are diffused through viscosity [17]. The integral scale is a measure of the average size of these larger eddies within a turbulent flow. Turbulent eddies at this length

scale are anisotropic and have large velocity fluctuations. The Taylor microscale represents the inertial subrange where turbulence is isotropic. The Kolmogorov scale characterizes the smallest turbulent eddy structures where the kinetic energy of these small eddies is dissipated through viscosity and converted into internal energy of the fluid [15]. The Kolmogorov scale eddies are the smallest turbulent structures present in the fluid flow.

CFD simulations must be able to spatially resolve the Kolmogorov length scale to completely capture and reproduce turbulent flow behavior. The Kolmogorov length scale is defined as

$$\eta = \left(\nu^3/\varepsilon\right)^{1/4} \tag{2.7}$$

where ν is the kinematic viscosity and ε is the dissipation of turbulent kinetic energy. The time scales associated with these length scales is

$$t_\eta = (\nu/\varepsilon)^{1/2} \tag{2.8}$$

Direct Numerical Simulation (DNS) is a high fidelity computational technique that resolves these spatial and temporal scales for all turbulent structures in a fluid flow; it is an extremely rigorous and accurate computational tool that requires large amounts of computing power [18][10]. The number of cells needed to accurately perform a DNS calculation scales with $Re^{9/4}$ [19]. This means that DNS requires large amounts of computing power because it requires the complete solving of the three-dimensional and time-dependent Navier-Stokes equations, making the use of DNS impractical for the study of most fluid flows [17]. However, even with the large computing power needed, DNS is a useful tool in the creation of data sets that will complement those generated by the DESTROJER test facility. The test facility is unable to collect data on the heat transfer between the fluid and impinging plate, so DNS methods developed by Pennsylvania State University will be used to create heat transfer data sets for future use in the validation of the STRUCT-ε model.

2.4 Turbulence Modeling

An array of turbulent modeling methods have been developed to reduce computational costs and widen CFD's applicability. These models seek to eliminate the need to deterministically simulate the smallest and most computationally expensive eddy structures by employing a diverse set of assumptions and equation closures.

2.4.1 Reynolds Averaged Navier Stokes

The most widely used modeling method for turbulent flow are the Reynolds Averaged Navier Stokes (RANS) equations. The RANS equations are a time averaged form of the Navier-Stokes equations and are appropriate for turbulent flows where the quantity of interest is the mean behavior of the flow and not the instantaneous fluctuations. The RANS equations solve for the average effect of turbulent quantities instead of the value of their instantaneous variation. These average quantities are often the value of interest in engineering applications of CFD, making RANS both appropriate and computationally cheaper [20].

In the RANS approach, velocity is decomposed into its means and its fluctuation in a process called Reynolds decomposition [15].

$$U = \overline{U} + U' \tag{2.9}$$

The averaged equations are then obtained by inputting the decomposed value of velocity into the Navier Stokes equation. The averaged equation is then found to be

$$\rho\frac{\partial\overline{U}}{\partial t} + \rho\bar{U}\cdot\nabla\overline{U} = -\nabla P + \nabla\left(2\mu S_{ij} - \rho\overline{u_j' u_i'}\right) \tag{2.10}$$

where $\rho\overline{u_j' u_i'}$ is the Reynolds stress tensor and the strain rate tensor, S, is defined as

$$S_{ij} = \frac{1}{2}\left(\frac{\partial\overline{U}_i}{\partial y} + \frac{\partial\overline{U}_j}{\partial x}\right) \text{[14]} \tag{2.11}$$

The Reynolds stress tensor is a symmetric matrix that represents the average

apparent stresses that result from fluctuations in velocity. The diagonal components of the Reynolds stress tensor represent the normal stresses while the off-diagonal components represent the shear stresses [15]. The Reynolds averaged flow equations are unclosed as they are a set of four equations containing ten total unknowns [17].

Eddy Viscosity Model

One method to determine the unknown Reynolds stress tensor is the use of an eddy viscosity model (EVM). Eddy viscosity models are based on the turbulent-viscosity hypothesis proposed by Boussinesq in 1877. According to the hypothesis the Reynolds stress is proportional to the mean rate of strain

$$\tau_{ij} = 2\mu_t S_{ij} - \frac{2}{3}\rho k \delta_{ij} \tag{2.12}$$

where τ_{ij} is the Reynolds stress tensor, μ_t is the eddy viscosity, and S_{ij} is the mean strain rate [15]. The Boussinesq hypothesis allows for the effect of turbulence on the mean flow to be treated analogously to the effects of viscosity on laminar flow, but there are many available models to solve for the eddy viscosity, μ_t.

k-ε Model

The most widely used model is the k-ε, a two-equation model that solves the turbulence transport equations for two additional quantities, the tubulent kinetic energy, k, and the turbulence dissipation rate, ε to solve for the eddy viscosity [15]. The Standard k-ε model was developed by Jones and Launder (1972) and is the basis for most applications today including STRUCT-ε [8][17]. Equations A.1 through A.4 in Appendix A.1 describe the Standard k-ε model. It is important to know that the transport equation for ε was not systematically derived, but instead developed as a direct analogy to and dimensionally consistent with the turbulent kinetic energy equation [17].

While the Standard k-ε model is one the most widely used and accepted turbulence models, it is neither the most accurate or computationally efficient method [17]. The

Standard k-ε model shows high level of inaccuracy for complex flow features such as strong pressure gradients and stream line curvature as the model assumes that the turbulent viscosity is isotropic. In cases where this assumption is not valid the use of non-linear eddy viscosity models (NLEVM) can enable the accurate calculation of secondary flows through their reintroduction of anisotropy in the flow [15][16].

One such NLEVM is the Cubic k-ε model developed by Baglietto and Ninokata (2006) which has been shown to be able to accurately reproduce secondary flows by using DNS data to adjust coefficient values and correct near wall damping [21]. The Cubic k-ε model is the basis of the STRUCT-ε model [22]. The complete transport equations of the Cubic k-ε model can be found in Appendix A.2. It is important to note that the turbulence transport equations for k and ε are the same in the Standard k-ε model as in the Cubic k-ε model, but now a quadratic stress-strain relationship is used to capture the sensitivity to normal stresses anisotropy [21].

k-ω Model

The k-ω model is another popular two-equation model. This model utilizes the specific turbulence dissipation rate, ω, in place of ε where

$$\omega = \frac{\epsilon}{k} \tag{2.13}$$

The most widely used k-ω implementation is the Wilcox k-ω, details of the complete model implementation are found in Appendix A.3. The k-ω model, unlike the k-ε model, maintains positive diffusion and thus physical validity near the wall [17].

Greater accuracy in the near wall region and improved consideration of stream-wise pressure gradients are the major strengths of the k-ω model. The k-ω model has some major weakness including its sensitivity to the turbulent inlet boundary conditions in the freestream and its over prediction of shear stress in the boundary layer [15][17].

The k-ω Shear Stress Transport (SST) model was proposed by Menter (1994) to capture both the k-ω model's high accuracy in the near wall region and the k-

ε model's superior performance far from the wall. The k-ω SST model utilizes a blending function to model the boundary layer using the k-ω model and the k-ε model in the free shear flow region [15].

2.4.2 Large Eddy Simulation

LES is a CFD turbulence modeling technique that utilizes spatial scale filtering to distinguish between the treatment of energy carrying large eddies and energy dissipating small eddies. LES uses a coarse spatial grid to solve the Navier-Stokes equations for large eddies while leaving the effect of small eddies to be captured using a sub-grid model [17]. LES accomplishes this by decomposing the velocity into a resolved component, $\overline{u}_i$, and a sub-grid component, u'_i.

$$u_i = \overline{u}_i + u'_i \tag{2.14}$$

The sub-grid model is then used to account for the momentum flux between the large and small scale eddies. The most widely used sub-grid model was proposed by Smagorinsky (1963) which utilizes the Boussinesq hypothesis where the sub-grid scale Reynolds stresses are calculated as

$$\tau_{ij} - \frac{1}{3}\tau_{kk}\delta_{ij} = 2\mu_t \overline{S}_{ij} \tag{2.15}$$

where μ_t is the eddy viscosity of the sub grid scale and $\overline{S}_{ij}$ is the strain rate of the resolved scale (Equation 2.11)[14].

The Smagorinsky model does not accurately capture the eddy-viscosity behavior near a wall [17]. The wall adapting local eddy (WALE) viscosity model was introduced to recover the proper near-wall behavior. This is done by relating the eddy viscosity to the velocity gradient tensor and strain rate tensor

$$\mu_t = (C_w\Delta)^2 \frac{(\overline{S}^d_{ij}\overline{S}^d_{ij})^{3/2}}{(S_{ij}S_{ij})^{5/2} + (S^d_{ij}S^d_{ij})^{5/4}} [23] \tag{2.16}$$

where $C_w = 0.544$, Δ is the grid size, and $\overline{S}_{ij}^d$ is

$$\overline{S}_{ij}^d = \overline{S}_{ik}\overline{S}_{kj} + \overline{\Omega}_{ik}\overline{\Omega}_{kj} - \frac{1}{3}\delta_{ij}(\overline{S}_{mn}\overline{S}_{mn} - \overline{\Omega}_{mn}\overline{\Omega}_{mn}) \tag{2.17}$$

where $\overline{S}_{ik}\overline{S}_{kj}$ is the rate of strain and $\overline{\Omega}_{ik}\overline{\Omega}_{kj}$ is the rate of rotation. The WALE model achieves correct near wall behavior by accounting for shear stress near the wall and has shown to provide results comparable to more computationally expensive sub-grid scale models [17].

LES is an intermediary between RANS and DNS. The explicit representation of large scale eddies enables LES to achieve higher accuracy by avoiding the broad averaging conducted in RANS. Meanwhile, the modeling of small scale eddies can significantly decrease computational cost as compared to DNS because a majority of the computational expense of DNS is needed for calculations related to the smallest scales [15].

LES models remain difficult to implement as their computational cost still requires that codes be purpose built for specific geometries [14]. LES calculations are highly dependent on the selected spatial filtering. The distinction between large and small eddies is defined by the user through grid selection; if the grid is too coarse then a majority of the turbulent energy resides in the sub-grid scale and cannot be accurately calculated using the Navier-Stokes equations. LES is also highly sensitive to boundary conditions, requiring very fine grids near walls to resolve the boundary layer which limits the potential computational savings from DNS [15].

2.4.3 Hybrid Models

Hybrid models seek to achieve a balance between the cost efficiency and robustness of RANS and the accuracy of LES methods. Many hybrid models have been proposed, but three of these models will be discussed to demonstrate the applications of hybrid models and some of the influences for the development of the STRUCT-ε model.

Detached Eddy Simulation

Detached Eddy Simulation (DES) was proposed by Philippe Spalart (1999) as a way to mitigate the shortcomings of LES and RANS [17]. DES utilizes RANS methods for the attached boundary layer and LES methods for the free shear flow in the separated region [14]. This approach provides computational cost savings by avoiding the use of a DNS like grid near the wall needed to separate small and large-scale eddies while allowing for an automatic transition without a defined boundary to eddy simulation away from the wall [17]. DES has demonstrated promising results on a variety of test cases, but has also displayed strong grid dependency and inconsistency. [24]

Scale Adaptive Simulation

The Scale Adaptive Simulation (SAS) model is a variation of the DES model based on the k-ω SST model proposed by Menter et al (2003). SAS uses the Von Karman length

$$L_{vK} = \kappa \left| \frac{S}{\nabla^2 \boldsymbol{U}} \right| \tag{2.18}$$

where the Von Karman constant $\kappa = 0.41$, to control the transition to and activation of eddy modeling [17]. The Von Karman length is a physical length scale derived from the local turbulence scale and allows greater flexibility in the SAS model as it is independent from the boundary layer thickness and grid size utilized by the standard k-ω SST model. The local turbulent length scale is then used for the smooth transition of calculations from an LES model for eddy resolution to a RANS model [25]. The SAS model has shown great success in external flow applications, but struggles with internal flows to the point that RANS solutions are sometimes more accurate [8].

Partially Averaged Navier-Stokes

The Partially Averaged Navier-Stokes (PANS) model devised by Girimaji (2004) controls the level of physical resolution through the use of f_k

$$f_k = \frac{k_u}{k} \tag{2.19}$$

the fraction of unresolved kinetic energy and f_e

$$f_e = \frac{\varepsilon_u}{\varepsilon} \tag{2.20}$$

the fraction of unresolved dissipation were k and ε are the RANS kinetic energy and dissipation respectively [26]. When f_k and $f_e = 1$, PANS produces the same result as a RANS calculation as almost all dissipation occurs in small turbulent structures which reach their average behavior rapidly [26]. When f_k is between zero and one, the turbulence dissipation equation is modified and hybridization occurs [10].

PANS has been shown to produce results that transition smoothly from RANS to DNS with increasing grid resolution, allowing for potential computational cost savings over LES while maintaining accuracy. However, the PANS implementation relies on a user defined resolution scale which enables inconsistent use of the model [26].

2.4.4 STRUCT-ε Model

The STRUCT-ε model is a hybrid model that combines RANS and Very-Large Eddy Simulation (V-LES) modeling methods. V-LES is an LES method where the spatial filter captures less than 80% of the total energy in the resolved large eddies. RANS struggles with accuracy because it is based on a simplified eddy viscosity, μ_t, calculation that over-estimates the eddy viscosity. The over estimated eddy viscosity then makes it difficult to accurately resolve complex or strongly fluctuating turbulent behaviors, the exact behaviors that define thermal striping [10]. The core basis of the STRUCT-ε model is the k-ε model which models μ_t as

$$\mu_t = C_\mu \frac{k^2}{\varepsilon} \tag{2.21}$$

where k is the turbulent kinetic energy, ε is the turbulent dissipation rate, and C_μ is a constant. To decrease the eddy viscosity a source term is added when calculating ε. This source term,

$$e_{source} = C_{3\varepsilon} \rho k Q_{abs} \tag{2.22}$$

increases ε, thereby decreasing eddy viscosity and the over-predicted stresses of the RANS model. $C_{3\varepsilon}$ is a constant chosen by sensitivity analysis, taken to be 1.5, and ρ is the density of the fluid [8]. Q_{abs} is the Q-Criterion and is the second invariant of the resolved velocity gradient tensor

$$Q = -\frac{1}{2}\frac{\partial \overline{u}_i}{\partial x_j}\frac{\partial \overline{u}_j}{\partial x_i} \tag{2.23}$$

The Q-Criterion is a measure of the presence of vorticity and thus can be used to identify turbulent eddies, which are composed of vorticies [27].

The STRUCT-ε model identifies hybridization regions by identifying regions of timescale overlap between the resolved and modeled turbulent structures, as opposed to the length scale reliance of SAS or the scaling coefficients of PANS [8]. This timescale overlap is identified by STRUCT-ε as regions where the Q-criterion is greater than ε/k, the turbulent eddy viscosity is then dynamically and implicitly modified by the e_{source} term [8]. The STRUCT-ε hybrid method benefits from its independence from inlet conditions, boundary conditions, and the grid [8].

Chapter 3

Methodology

3.1 STRUCT-ε Implementation

STRUCT-ε benefits from its straightforward implementation and wide applicability to engineering applications [8]. The STRUCT-ε model is based on the Cubic k-ε detailed in Appendix A.2 and utilizes the coefficients proposed by Baglietto and Ninokata tabulated in Table A.1. Complete implementation of the STRUCT-ε model requires the activation of a turbulent dissipation rate source term (Equation 2.22) used when calculating ε.

3.2 LES Implementation

The high accuracy of LES and its extensive validation enable the use of LES as a reference solution in the absence of experimental results. LES simulations are implemented as described in Section 2.4.2; complete details of the model implementation can be seen in Appendix A.4.

3.3 Modeling Parameters

All simulations conducted in this research project were completed as transient solutions, necessitating the choice of an appropriate time step. For each simulation, the

time step was chosen so that the Courant Number,

$$C = \frac{u\Delta t}{\Delta x} \tag{3.1}$$

is approximately 1.0 throughout the fluid domain to ensure numerical accuracy of the solution, where u is the local fluid velocity, Δx is the grid spacing, and Δt is the time step [14]. The details of all other parameters selected for each simulation, such as grid spacing, are detailed in their appropriate sections.

3.4 Evaluation Criteria

Experimental setups are evaluated on two conditions important to the analysis of thermal striping: the Root Mean Square (RMS) of Temperature and a frequency analysis of Temperature Signals though the use of Fast Fourier Transforms (FFT) and Proper Orthogonal Decomposition (POD).

3.4.1 Root Mean Square of Temperature

The RMS of temperature is an important figure of merit because thermal striping is most likely to occur in regions with large surface temperature fluctuations [5]. The RMS of temperature is a measure of the magnitude of temperature fluctuation.

The name RMS is a slight misnomer in the field of thermal-hydraulics as the quantity of interest is actually the standard deviation of temperature, the misnomer stems from the fact that the RMS of a quantity with a mean of zero is equivalent to its standard deviation. The RMS of temperature, T_{RMS}, is calculated as

$$T_{RMS} = T_{var} \tag{3.2}$$

where T_{var} is the variance of temperature with

$$T_{var} = \frac{1}{N}\sum_{n=1}^{N}\left(T_n - \overline{T}\right) \tag{3.3}$$

where N is the total number of temperature measurements, T_n is the instantaneous temperature, and $\overline{T}$ is the average temperature.

3.4.2 Proper Orthogonal Decomposition

Turbulent fluid flow is described by complex, random vector fields. PODs seek to decompose the random vector field $\boldsymbol{u'}(\boldsymbol{x}, t)$ into a series of spatial functions $\Phi_k(x)$ modified by time coefficients $a_k(t)$ that reveal coherent structures within the flow behavior [28].

$$\boldsymbol{u'}(\boldsymbol{x}, t) = \sum_{k=1}^{\infty} a_k(t)\, \Phi_k(x) \tag{3.4}$$

$\Phi_k(x)$ represent the POD spatial modes, with lower modes capturing a greater portion of the total kinetic energy. Thus the first POD mode corresponds to the strongest oscillatory signal. Results of POD analysis will be used to determine the presence of oscillatory flow behavior and the frequency of such behavior.

3.4.3 Fast Fourier Transform of Temperature Signals

FFTs are a form of spectral analysis that determine the frequencies present in a signal by decomposing the signal in the time domain into its individual frequency components. FFTs are a discrete Fourier transform (DFT) that utilizes redundant calculations to decrease calculation time [29]. The coefficients of a DFT are a measure of the relative strength of a frequency signal and are calculated as

$$F(k) = \frac{1}{\sqrt{N}} \sum_{n=0}^{N-1} f(n)\, e^{-j2\pi kn/N} \tag{3.5}$$

where k is the wavenumber and N is the total number of samples.

Thermal striping occurs during temperature fluctuations between 1 and 50 Hz, with frequencies below 10 Hz being especially damaging [30]. Results of FFT analysis will be evaluated qualitatively to determine if the frequencies present represent frequencies with a higher risk of thermal striping.

Chapter 4

Jet Behavior Modeling

This chapter will review the modeling parameters, process, and geometries used in the development of experimental test cases to be conducted at the DESTROJER test facility shown in Figure 2.1. An analysis of the simulation results of each geometrical configuration is detailed for the purpose of guiding the determination of experimental test cases to be performed and the geometrical configuration to be used.

4.1 Flow Geometry

The fundamental flow case consists of two symmetric jets impinging orthogonally onto a smooth, flat plate. The cold jet issues air at ambient temperature and the hot jet issues heated air from circular pipes of inner diameter $1D$ and outer diameter $1.25D$, where D is 1 inch. In the DESTROJER test facility, the jets have a length of $66.5D$ through which the flow develops. To reduce size of the computational domain needed to simulated the DESTROJER test facility, the length of the circular pipes were shortened to $7.42D$. This is the total length of the circular pipes contained within the bulk fluid domain. Section 4.5 provides a complete description of the inlet flow conditions used to ensure fully developed boundary conditions in the jet pipes despite the geometric reduction of the fluid domain.

The DESTROJER test facility was recreated in CAD, a transparent view of which can be seen in Figure 4.1. A few geometric simplifications have been made to reduce

the complexity and size of the fluid domain. The outlet valves were simplified to cylinders, the bottom of the fluid domain was raised to the plate that the jets protrude from, and the impingement plate was reduced to a rectangular prism. The adjustments to the outlet valves and base of the fluid domain are far from the impingement plate where the figures of merit are being evaluated. The lower face and thickness of the impingement plate are unaffected, leaving the fluid flow in the region of interest and the thermal response of the acrylic unchanged. All three simplifications provide computational savings while having negligible impact on the flow quantities of interest.

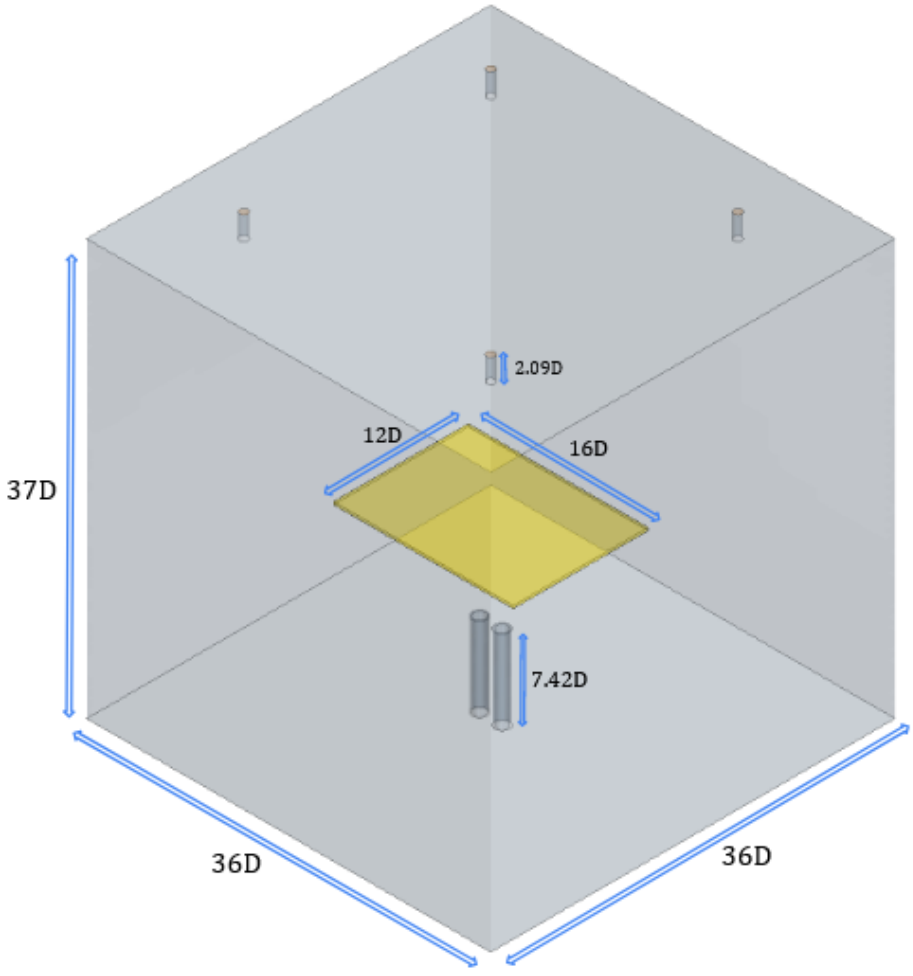

Figure 4.1: Transparent view of CAD geometry used to simulate the fluid volume of the DESTROJER test facility. Notable geometric dimensions are labeled.

4.2 Modeling Parameters

4.2.1 Material Selection and Properties

The simulant fluid released from the jets was selected to be air by the experimentalists at the DESTROJER test facility; air was selected due to its ease of use and cost efficiency, and was simulated as an ideal gas to minimize computational cost while using temperature dependent properties. The thermal physical properties of air were used for all simulations are tabulated in Table 4.1.

Dynamic Viscosity (μ)	$1.85508 * 10^{-5}$ Pa-s
Molecular Mass (MM)	28.9664 g/mol
Specific Heat (c_p)	1003.62 J/kg-K
Thermal Conductivity (K)	0.0260305 W/m-K
Turbulent Prandtl Number (Pr_t)	0.9

Table 4.1: Thermal physical properties of air.

The fluid released from the jets is characterized by a molar flow rate measured in standard liters per minute (SLPM). One SLPM is 0.73386 mmol/s which at the thermal physical properties selected is equivalent to $2.12573 * 10^{-5}$ kg/s. Two jet inlet conditions were used while testing the geometrical configurations which are detailed in Table 4.2.

Cold Jet Temperature	Hot Jet Temperature	Cold Jet Flow Rate	Hot Jet Flow Rate
20 °C	45 °C	160 SLPM	160 SLPM

Table 4.2: Jet inlet conditions used for DESTROJER simulations.

The impingement plate is made from cast acrylic, the thermal physical properties of the impingement plate were taken from the manufacturer and can be found in Table 4.3. Thermal physical properties defined as a range were taken as the central value of the range.

Density (ρ)	0.043 lb/in^3
Specific Heat (c_p)	1810.0 J/kg-K
Thermal Conductivity (K)	0.198 W/m-K

Table 4.3: Thermal physical properties of cast acrylic [31][32].

4.2.2 Boundary Conditions

The four outlet valves have a diameter of $0.72D$ and were modeled using a defined boundary pressure of 0 Pa. The six walls of the impingement plate were simulated as no-slip walls with mapped contact interfaces and implicit energy coupling. All other walls were simulated as adiabatic, no-slip walls. An adiabatic thermal specification was selected for these walls due to the negligible heat transfer expected and to minimize their impact on the solution; thermal striping caused by interactions between the jets is the phenomena of interest.

4.3 Meshing Details

For all simulations presented in this work, the DESRTOJER fluid domain was discretized using an automated trimmed cell mesher. The mesh scale selection was informed by an investigation of the integral length scales

$$\mathcal{L} = \frac{k^{3/2}}{\varepsilon} \tag{4.1}$$

where k is the turbulent kinetic energy and ε is the turbulence dissipation rate, is shown in Figure 4.2 from a precursory RANS simulation. This simulation used the flow conditions detailed in Table 4.2 and a placement of the impingement plate such that the lower face was located $19.42D$ from the top of the jet pipes. See Section 4.4 for a complete overview on the placement selection of the impingement plate.

The mesh base size should be as large as possible to decrease the computational cost, but small enough to ensure accuracy of the STRUCT-ε model. Studies on the interaction of symmetric jets at the RCCS test facility have shown that STRUCT-ε achieves solution accuracy when the mesh size was equal to $\mathcal{L}/2$ [11]. To achieve a

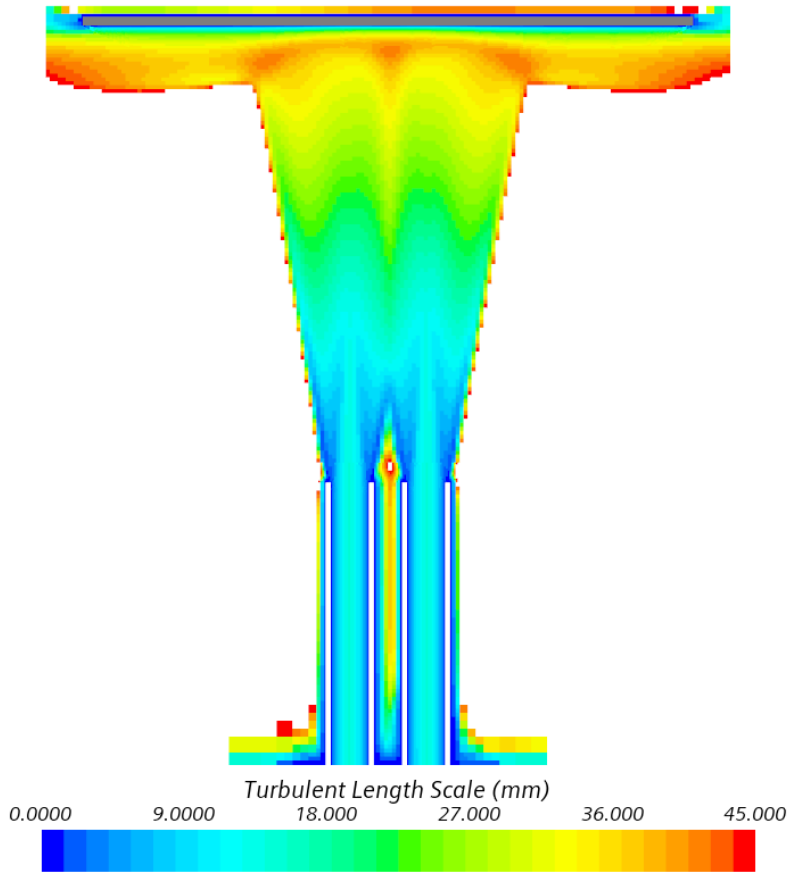

Figure 4.2: Integral length scales below the impingement plate in the y-z plane of the fluid domain from precursory RANS simulation.

grid size of $\mathcal{L}/2$, a base mesh size of 21.2mm was selected and two volumetric control regions were used to refine the mesh further.

The first mesh refinement region was applied to the fluid region under the impingement plate and above the outlets of the jets. The region, pictured in Figure 4.3, is defined by a conical frustum with lower radius width $2.75D$, upper radius $10D$, height $12D$, and extends between the impingement plate and $7.42D$ above the base of the fluid domain.

In this refinement region, the mesh was refined to 12.5% of the base mesh size. The impingement plate was modeled using 34 prism layers with a near wall thickness of 0.02mm and a total thickness of 25mm. The number of prism layers and near wall thickness was selected to minimize the computational cost while minimizing the

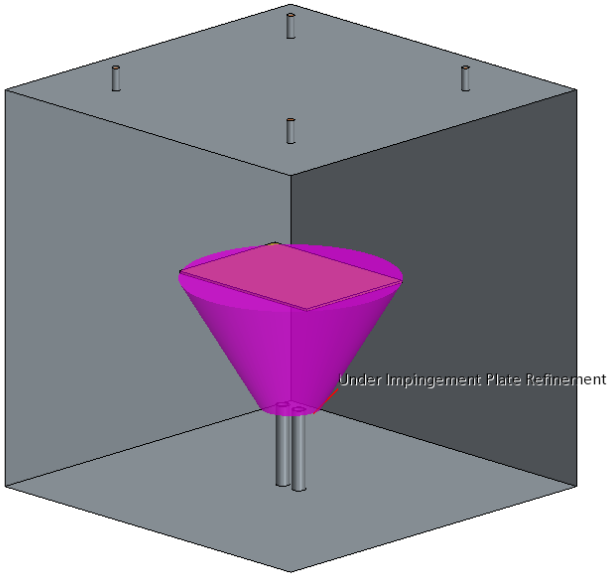

Figure 4.3: Mesh refinement region applied to the region between the impingement plate and jet outlets.

numerical error from the low-Re wall treatment described in Section 4.5.2 and to achieve a wall $y+$ of less than 1.

$$y+ = \frac{u_\tau y}{\nu} \tag{4.2}$$

where y is the wall distance, ν is the kinematic viscosity, and u_τ

$$u_\tau = \sqrt{\frac{\tau_w}{\rho}} \tag{4.3}$$

is the friction velocity with τ_w being the wall shear stress. The wall y+ is a non-dimensionalized measure of wall distance. A wall y+ of less than 1 is sought as this is a requirement in the first prism layer for the low-Re wall treatment [33]. The decision to use the low-Re wall treatment was based on an earlier analysis of STRUCT-ε that found that it was better suited to resolving the turbulent structures of interest in the DESTROJER test facility [13].

The other mesh refinement region was applied to the pipes that the jets enter the free volume of the fluid domain and the region immediately above the jets. The region, pictured in Figure 4.4, is defined by two cylinders within the jets with diameters of $1D$ and height $7.38D$ and by a cylinder with diameter $1.97D$ and height $0.5D$. In

this second refinement region, the mesh was refined to 6.25% of the base mesh size. The walls were of the jets were modeled using 34 prism layers with a total thickness of 4.5mm. These refinements were done to ensure accurate representation of the inlet velocity profiles for the two jets.

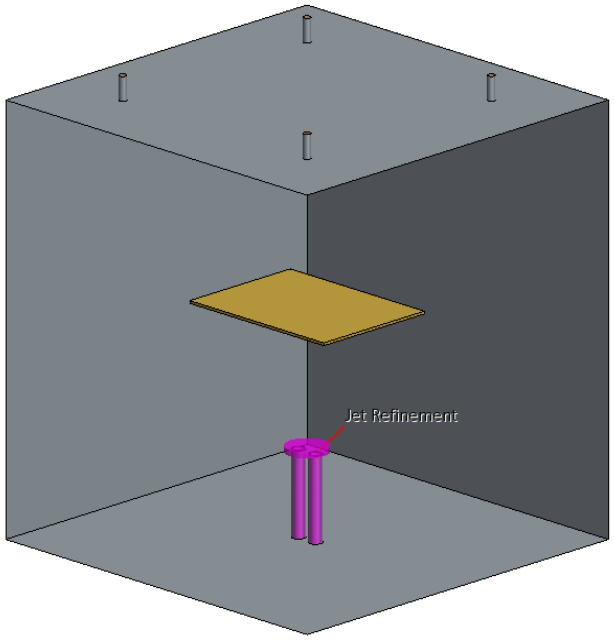

Figure 4.4: Mesh refinement region applied to inlet jets and cylindrical region directly above the jet outlets.

Outside of these refinement zones, the base mesh size is used to discretize the fluid domain. The accuracy of the solution far from the jet profiles and impingement plate is not of utmost importance, so the prism layers on the outer walls were disabled. A view of the mesh can be seen in Figure 4.5. Complete meshing details are tabulated in Table 4.4.

4.4 Impingement Plate Placement

Four different impingement plate placements were used in the course of this study. The size of the impingement plate remained constant across all simulations.

The first impingement plate placement used is $12D$ above the top of the jet exits and orthogonal to the jet flow. This placement can be seen in Figure 4.1. The other

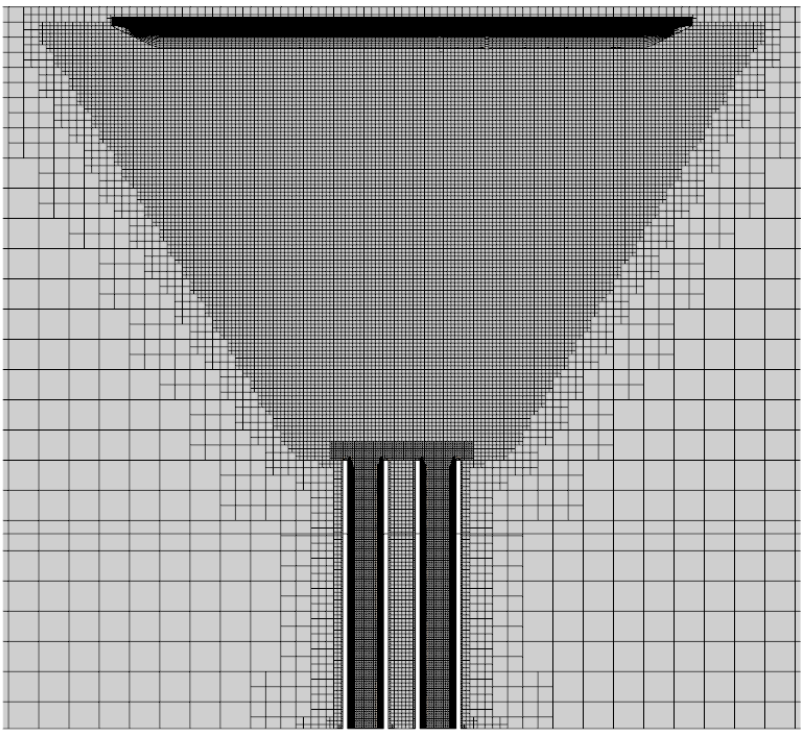

Figure 4.5: View of x-z plane cross section of the mesh created to simulate the DESTROJER test facility geometry.

Mesh Details		
Fluid Domain	Base Size	21.2mm
Impingement Plate	# of Prism Layers	34
	Prism Layer Near Wall Thickness	0.02mm
	Prism Layer Total Thickness	25mm
	Mesh Refinement	12.5%
Jets	# of Prism Layers	34
	Prism Layer Near Wall Thickness	0.02mm
	Prism Layer Total Thickness	4.5mm
	Mesh Refinement	6.25%
Outlets	# of Prism Layers	21
	Prism Layer Near Wall Thickness	0.05mm
	Prism Layer Total Thickness	3.0mm
	Target Surface Size	6.25%

Table 4.4: Meshing details for the DESTROJER simulations, percents represent percentage of the base mesh size.

three impingement plate location used were $20D$, $6D$, and $2D$ above the jets exits and orthogonal to the jet flow. These configurations were selected to study how varying distance from the jet outlets, and thus time allowed for interactions between the jets, would influence thermal striping phenomena.

4.5 Solution Methods

4.5.1 Jet Inlet Conditions

As mentioned in Section 4.1, the fluid at the DESTROJER test facility first travels through a pipe of length $66.5D$ before exiting the jets to ensure that the jet has a fully developed velocity profile. Directly simulating the entire flow development length in the simulations presented in this work would be too computationally expensive. To decrease the computational intensity, a separate simulation conducted on a shortened length, $7.42D$, of pipe with periodic flow boundary conditions was carried out in isolation to reproduce the fully developed jet inlet conditions.

Further reduction of the computational intensity was achieved by running the simulation at steady state. After 14,000 iterations, the flow converged to fully developed condition. The velocity, turbulent kinetic energy, and turbulence dissipation rate profiles at the inlet of each of the jets were extracted and used as the inlet conditions. The mesh elements of the pipe segment and jet inlet were matched to minimize the numerical error from this process.

4.5.2 Simulation Implementation

The STRUCT-ε model was implemented with a low-Re wall treatment to resolve the viscous sublayer [34]. A complete description of the low-Re approach implementation can be found in Appendix A.1.1.

All simulations conducted in this work were run in two stages; the first stage is completed at steady state and the second stage is completed as a transient simulation. The steady state stage was run for 25,000 iterations to initialize the flow conditions

and decrease the time the transient had to run before data collection started.

The transient stage for jet behavior modeling was then completed with a time step of $1 * 10^{-4}s$, a total run time of 60.0s, and data collection for FFT and RMS of temperature analysis occurring between 30.0 and 60.0s. Data collection for POD analysis occurs every 1.0ms between 50.0 and 60.0s due to the higher amount of computational power needed to produce POD analysis. The Courant number scene displayed in Figure 4.6 demonstrates that a $1 * 10^{-4}s$ time step is appropriate for achieving a Courant number of approximately 1.0 throughout the fluid domain. A total time of 60.0s was selected based on limitations of the available computing power. Data collection started at 30.0s to ensure complete development of flow behavior and properly analyze thermal striping phenomena that may be present.

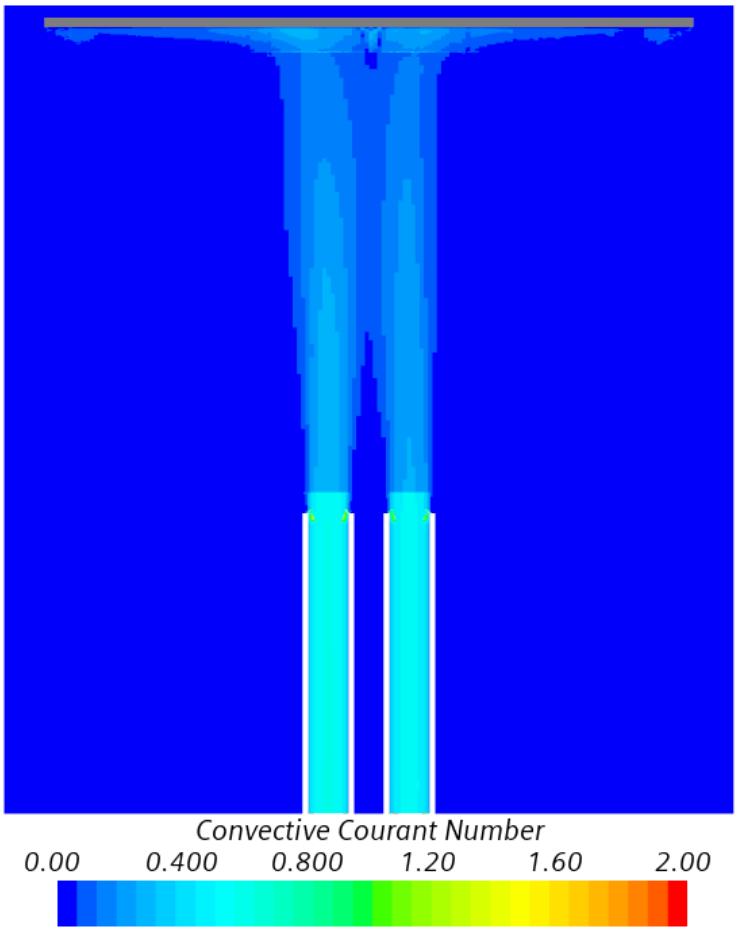

Figure 4.6: Courant number on x-z plane with a time step of $1 * 10^{-4}s$.

4.6 Expected Flow Behavior

A single impinging jet was used for validation of the STRUCT-ε model by Yau (2019) [10]. The fundamental phenomena studied in this work is a two jet configuration which introduces additional complexity.

Multi-jet impingement has two interactions that are unique from single jet impingement. The first is interference between the jets prior to impingement; this is more likely when the jets are relatively close together or relatively far from the impingement surface [35]. Jet interference behavior can be see in Figure 4.7. The second is collision of the jets' surface flow along the impingement surface which is more likely when the jets are relatively close together, close to the impingement surface, or with relatively high jet velocity [35]. Jet collision and up-wash flow behavior can be seen in Figure 4.8.

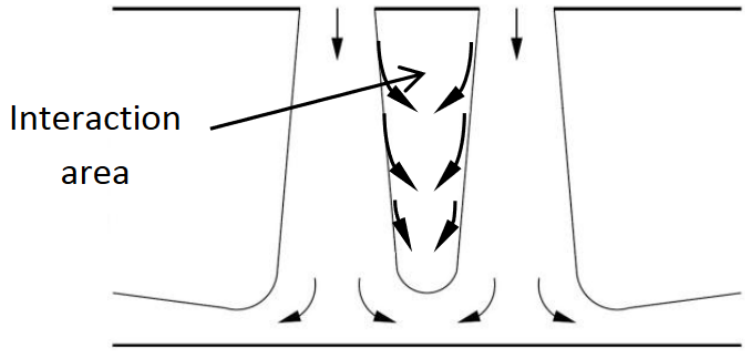

Figure 4.7: Interference between two jets in a multi-jet impingement system [36].

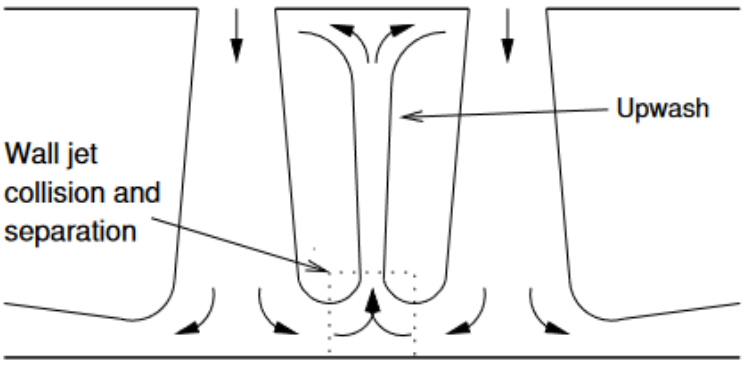

Figure 4.8: Jet collision and up-wash flow behavior of a two jet impingement [37].

Interference between the jets is the desired flow behavior as thermal striping results from oscillatory mixing. The distance to the impingement plate is the only variable across the test cases; the distance between jets and the jet velocity is unchanged throughout all test cases. It is expected then that the higher impingement plate locations will most likely induce thermal striping behavior. However, the high jet velocity has the potential to sustain jet collision and down-wash in all test cases.

4.7 Results and Discussion

4.7.1 Flow Behavior

The average velocity in the z direction can be seen in Figure 4.9 for the four impingement plate placements. The $2D$ and $6D$ cases display down-wash flow behavior with a large area of negative z velocity present between the jets near the impingement plate. The conical shape and overlap of the average z velocity profile seen in the $12D$ and $20D$ cases imply the presence of oscillatory behavior caused by jet interference. The transition to jet interference with greater impingement plate distance was the expected behavior and provides an initial demonstration of the STRUCT-ε model's ability to accurately represent the fundamental flow behavior being investigated.

The development of jet interference with greater impingement plate distance can also be seen by looking at the temperature variance (Equation 3.3), as shown in Figure 4.10. In the $2D$ and $6D$ impingement plate configurations the area of peak temperature variance is contained between the two jets. Meanwhile for the $12D$ and $20D$ impingement plate distances, the area of notable temperature variance expands to the outside of the jet profiles. In the $20D$ case the location of the peak temperature variance moves away from the impingement plate as mixing is occurring between the jets. Peak temperature variance is also seen to decrease with increasing impingement plate distance as mixing occurs over a greater volume with increasing jet interference.

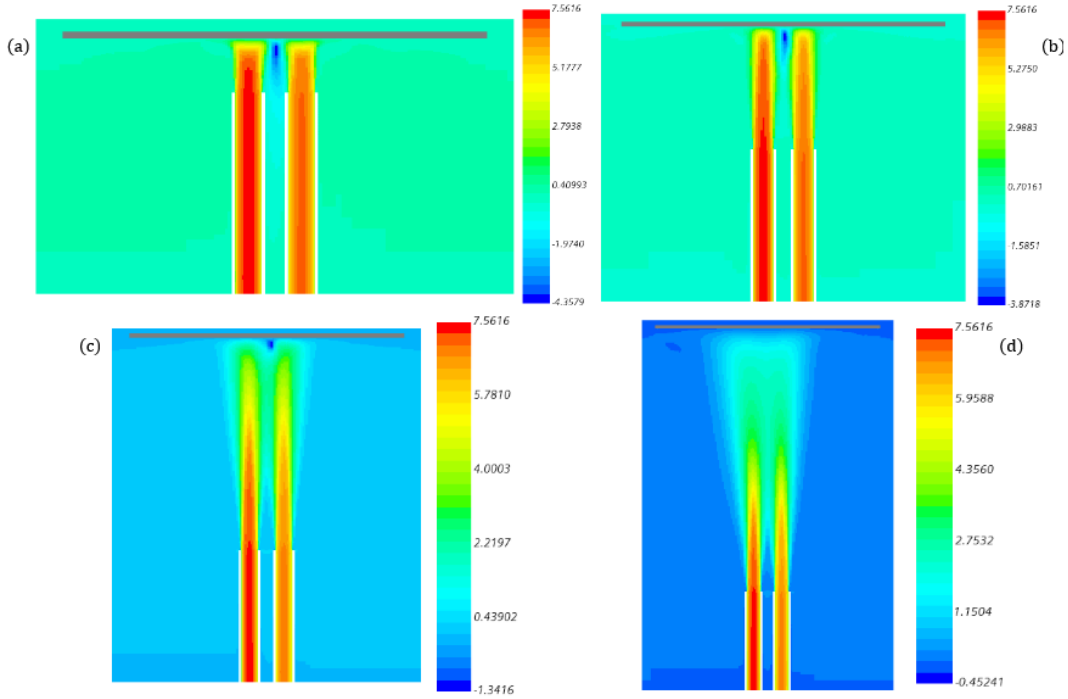

Figure 4.9: Average velocity in the z direction seen on the x-z plane for (a) $2D$, (b) $6D$, (c) $12D$, and (d) $20D$ impingement plate configuration.

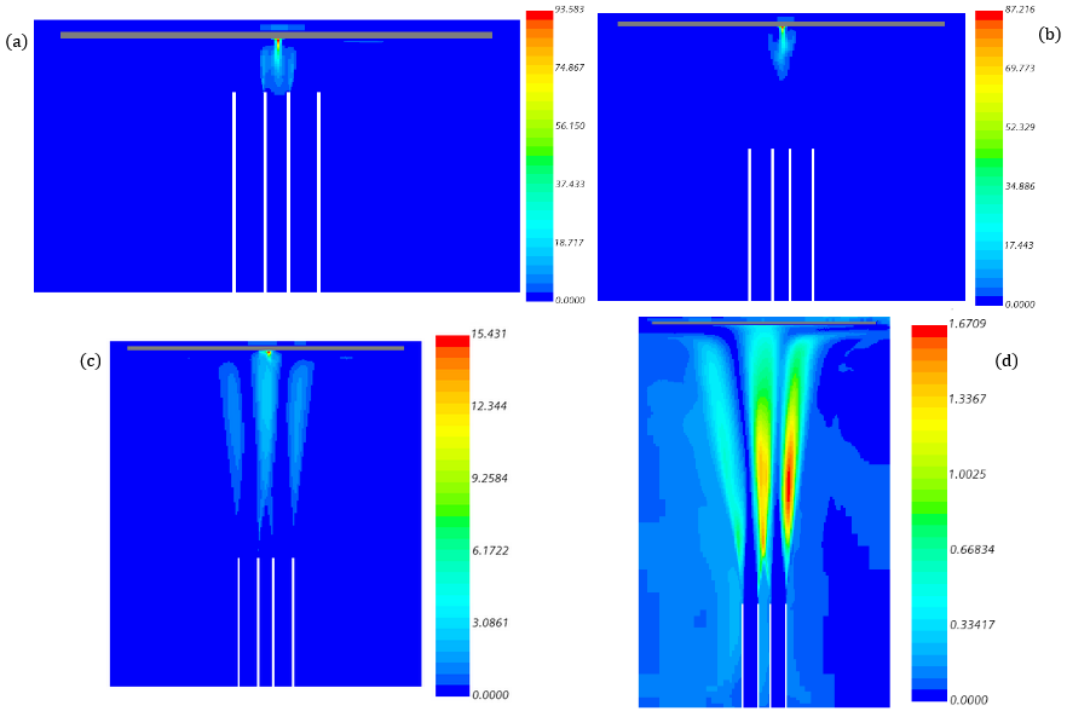

Figure 4.10: Variance of temperature on the x-z plane for the (a) $2D$, (b) $6D$, (c) $12D$, and (d) $20D$ impingement plate configuration.

4.7.2 Temperature Variance at Impingement Plate

Temperature variance at the impingement plate is of special importance as thermal striping is a phenomena experienced by solid components of reactors analogous to the impingement plate.

The temperature variance measured in the impingement plate profile at a height equal to the TCs described in Section 2.1 is displayed in Figure 4.11. Maximum temperature variance decreases while the width of the area of notable temperature variance increases with increasing impingement plate distance. A 2D view of this behavior is provided in Figure 4.12 where the RMS of temperature is measured along the optical fiber. In the design of experiments for the DESTROJER test facility, a balance between high temperature variance and a broad temperature variance region is desired. High temperature variance is necessary to produce significant thermal striping behavior while a broad region both implies oscillations between the jets, but decreases the risk of not capturing all important phenomena due to physical limitations of the data collection equipment.

The importance of temperature variance at the impingement plate makes the STRUCT-ε models performance at the wall vital. The Q-Criterion isosurface of 100 s^{-2} displayed in Figure 4.13 represents the turbulent structures generated by STRUCT-ε. With an impingement plate distance of $2D$ and $6D$ turbulent roll structures are visible along the impingement plate. Turbulent structures are visible in the $12D$ and $20D$ cases, but there are less defined structures at the impingement plate likely due to more dissipation occurring before the wall due to jet interference.

4.7.3 POD Analysis

As discussed in Section 3.4.3 the frequency of temperature oscillations is also a vital component of thermal striping. POD analysis is performed on a region defined by the x-z plane bound by the impingement plate and $0.5D$ above the jets in the z direction and between $-4.5D$ and $4.5D$ in the x direction. This relatively small region is utilized due to the high computational requirements of POD analysis.

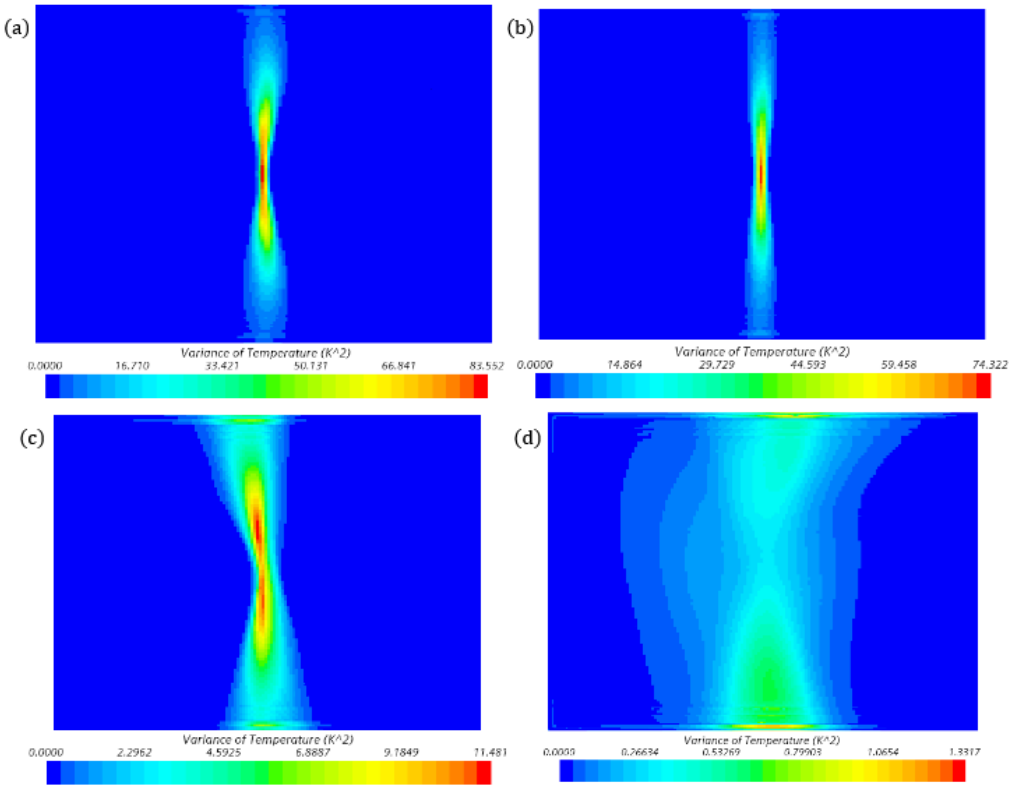

Figure 4.11: Variance of temperature on the TC plane under the (a) $2D$, (b) $6D$, (c) $12D$, and (d) $20D$ impingement plate configuration.

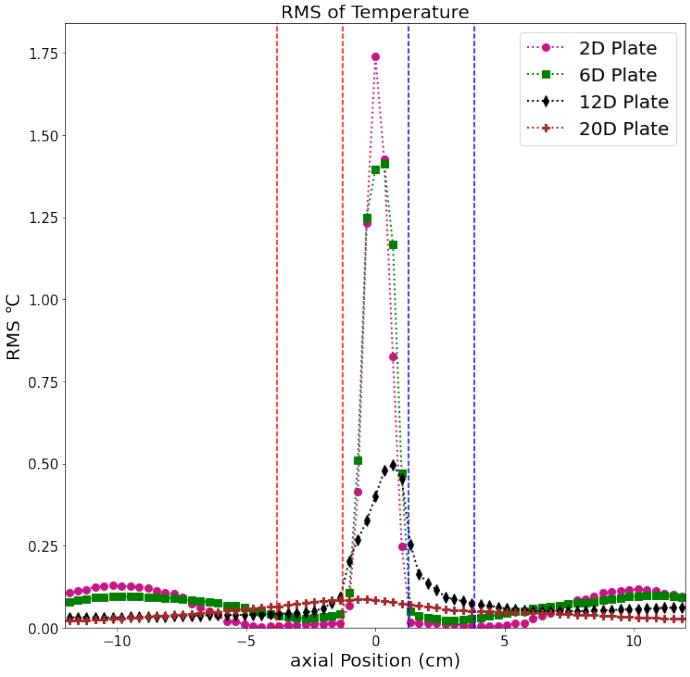

Figure 4.12: Comparison of the RMS of temperature measured along the optical fiber for the $2D$, $6D$, $12D$, and $20D$ impingement plate distances.

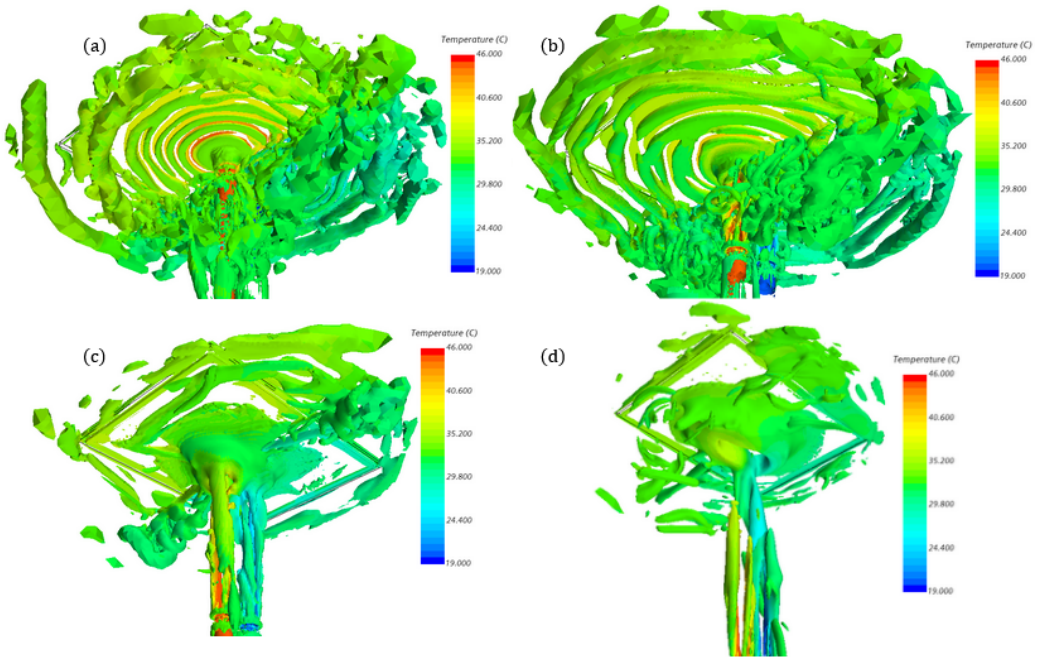

Figure 4.13: Temperature displayed on a Q-Criterion = 100 $/s^2$ iso-surface for the (a) $2D$, (b) $6D$, (c) $12D$, and (d) $20D$ impingement plate configuration.

Results of the first POD mode analysis are seen in Figure 4.14. The $2D$ case is seen to have little to no oscillatory behavior while the $6D$ case displays some minor velocity oscillations near the impingement plate, but temperature oscillations necessary for thermal striping only occurring in a small area. The $12D$ cases demonstrates strong oscillatory that extends nearly the whole length of the analysis window. Meanwhile the $20D$ case has similarly strong oscillations, but it appears to be dominated by the cold jet.

The oscillatory frequency of these POD modes are measured by the Power Spectrum Density (PSD) and are displayed in Figure 4.15. The $2D$ configuration appears to have a dominant frequency around 30 Hz while the $6D$ configuration has a peak frequency around 20 Hz. The $12D$ and $20D$ configurations show less defined oscillation frequencies around 1 Hz.

All four configurations demonstrated oscillatory frequencies in the range of interest for thermal striping. To confirm the oscillatory frequencies present FFT analysis was then performed at the 32 TC locations. Representative FFT results are presented in Figure 4.16. The FFT analysis confirms the presence of a 30 Hz and 20 Hz flow

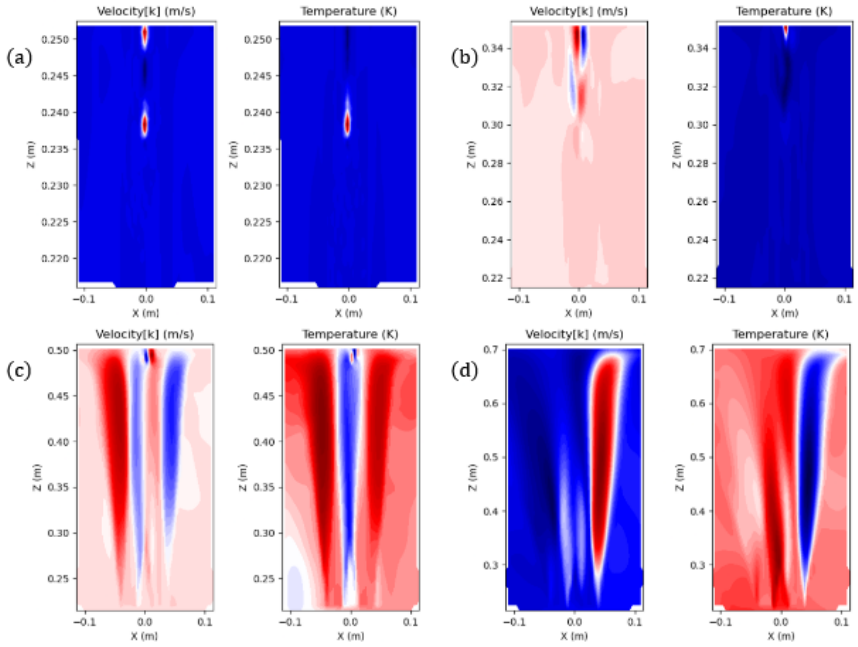

Figure 4.14: First POD mode of z velocity and temperature on the x-z plane between the impingement plate and $0.5D$ above the jets for the (a) $2D$, (b) $6D$, (c) $12D$, and (d) $20D$ impingement plate distances.

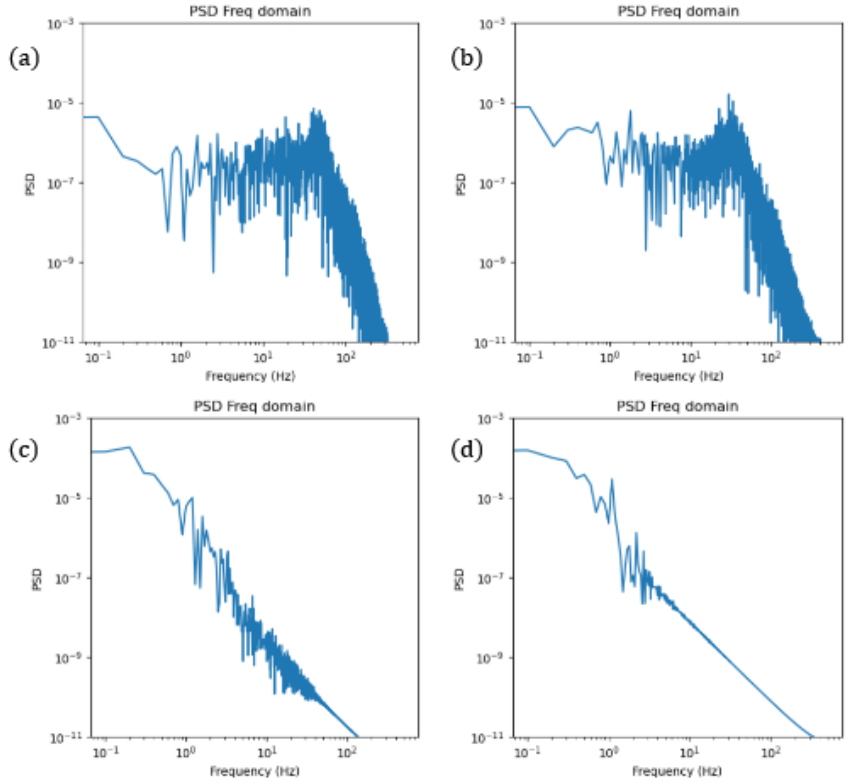

Figure 4.15: PSD frequency domain of first POD mode for the (a) $2D$, (b) $6D$, (c) $12D$, and (d) $20D$ impingement plate configurations.

oscillation frequency for the $2D$ and $6D$ impingement plates respectively. The $12D$ impingement plate was found to have multiple distinct oscillatory frequencies between 1 and 100 Hz peaks. Oscillatory behavior of 1-50 Hz is present, but they are of roughly equal strength and are therefore not readily apparent in the PSD frequency measurement. The FFT analysis of the $20D$ impingement plate does agree with the PSD measurement, continuing the implication that the jets are too well mixed by the time they reach the impingement plate for thermal striping to occur.

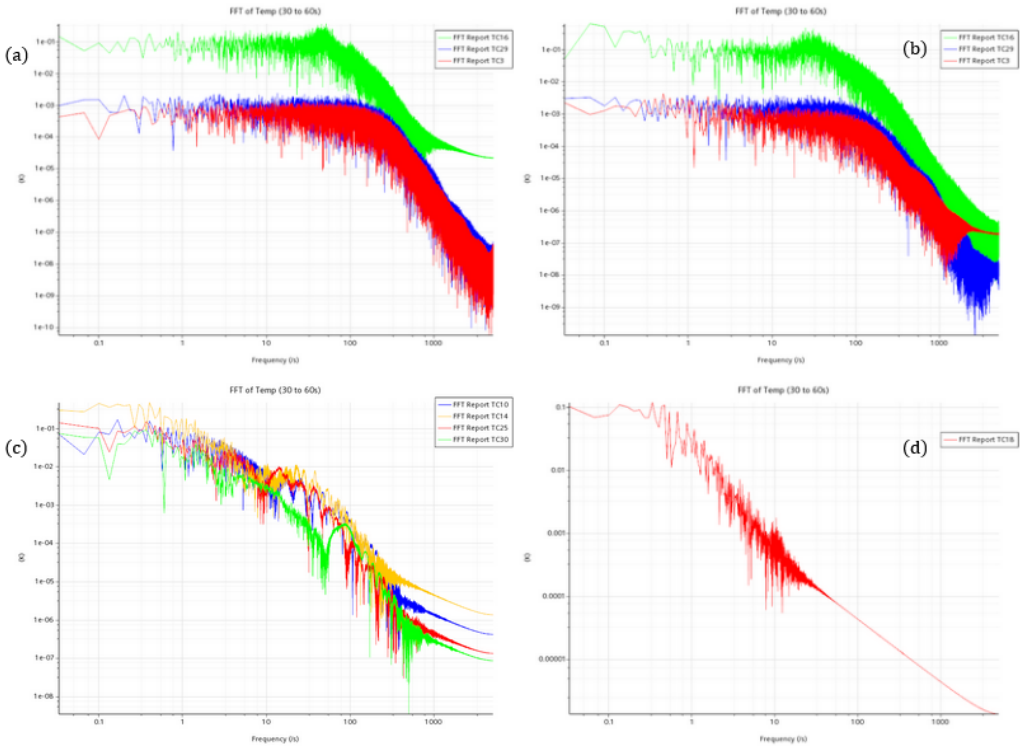

Figure 4.16: Representative temperature FFT coefficients versus frequency at the TCs for (a) $2D$, (b) $6D$, (c) $12D$, and (d) $20D$ impingement plate distances.

Chapter 5

Mixing of Jets Induced by Flow Past a Cylinder

The current DESTROJER test facility configuration has shown an overall lack of mixing between jets and low temperature variance along the impingement plate. The extremely localized flow and temperature oscillations make it an unsuitable configuration for validating thermal striping modeling approaches. To create an oscillation frequency between the jets a cylindrical obstacle impeding flow is added. The STRUCT-ε model is used to evaluate if the obstacle is able to successfully induce oscillations. LES is then used to confirm the findings and to compare the LES and STRUCT-ε model's predictions.

The $12D$ impingement plate placement was selected for the obstacle study as it provides the best balance between magnitude of temperature variance, desired oscillatory frequency, and size of oscillatory area while providing enough space to enable the placement of a flow obstruction.

5.1 Obstacle Geometry

The flow case geometry is the same as described in Section 4.1 except for the presence of the cylindrical obstacle. The cylindrical obstacle is centered between the two jets at a height of $3.75D$ above the jet exits and spans the complete $36D$ distance between the

walls of the fluid domain. Two obstacle diameters were used to test the performance of the STRUCT-ε model: $3.5D$ and $1.75D$. A view of the $3.5D$ obstacle configuration can be seen in Figure 5.1.

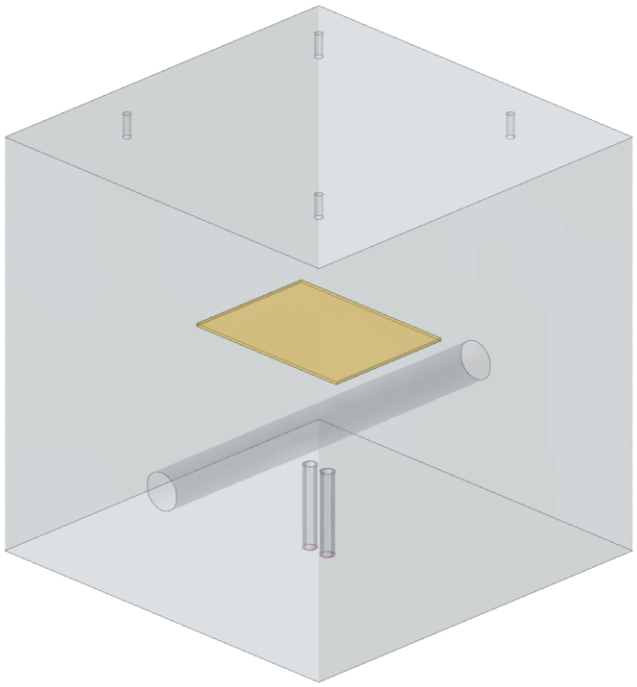

Figure 5.1: Transparent view of CAD geometry of the DESTROJER test facility with 3.5D diameter cylindrical obstacle.

5.2 Modeling Parameters

The modeling parameters are unchanged from those described in Section 4.2. The obstacle is modeled as an adiabatic, no-slip wall as heat transfer with the obstacle is expected to have negligible impact on the solution.

5.3 Meshing Details

The mesh utilized for all simulations with the STRUCT-ε model is the same as that described in Section 4.3. Within the conical frustum volume shown in Figure 4.3 the obstalce is meshed with a prism layer mesh of 42 prism layers with a near wall

thickness of 0.02mm and a total thickness of 15.0mm. A view of the obstacles prism layer mesh can be seen in Figure 5.2. Outside of the conical frustum the obstacle is meshed with a prism layer mesh of 5 prism layers with a near wall thickness of 0.02mm and a total thickness of 4.5mm. This courser mesh is used to minimize the computational expense in regions far from the area of interest.

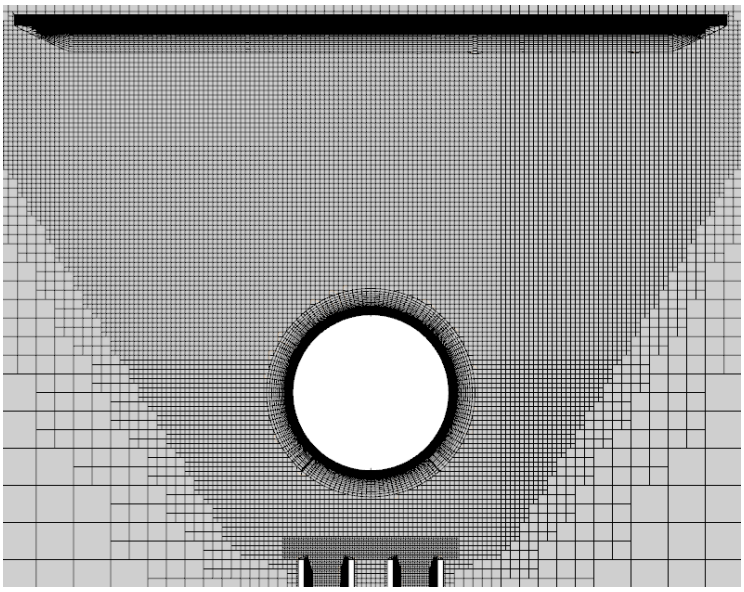

Figure 5.2: View of the x-z plane cross section of the mesh used to simulate the wall behavior around the flow obstacle.

5.3.1 LES Meshing Details

The grid size used in LES determines the size cutoff for resolving vs modeling eddies. The choice of grid size must balance the computational expense of a fine mesh with the level of accuracy desired. A grid size of $\mathcal{L}/6$ is selected for LES studies in this work so that the spatial filter captures 80% of the total turbulent kinetic energy in the resolved eddies [15]. A base mesh size of 21.2mm selected with one volumetric control region used to further refine the mesh.

The mesh refinement region used for LES combines the two regions used for the STRUCT-ε simulations described in Section 4.3 and is defined by a conical frustum and the jet pipes. Within this refinement region the mesh was refined to 6.25% of the base mesh size. The obstacle in this region was modeled using 65 prism layers with

a near wall thickness of 0.05mm and a total thickness of 15mm. The prism layer was selected to minimize computational cost while ensuring a wall $y+$ of less than 1 and a growth rate of less than 1.1 as these are requirements for accurate LES results near the wall [38].

Outside of this refinement region, the fluid domain is discretized the same as the STRUCT-ε simulations described in Section 4.3. Additionally, the jet pipes are shortened to a length of $1D$ to reduce computational expense while still allowing time for the flow to develop in the pipe. A view of the mesh used in the $1.75D$ diameter obstacle case can be seen in Figure 5.3 and complete meshng details are tabulated in Table 5.1.

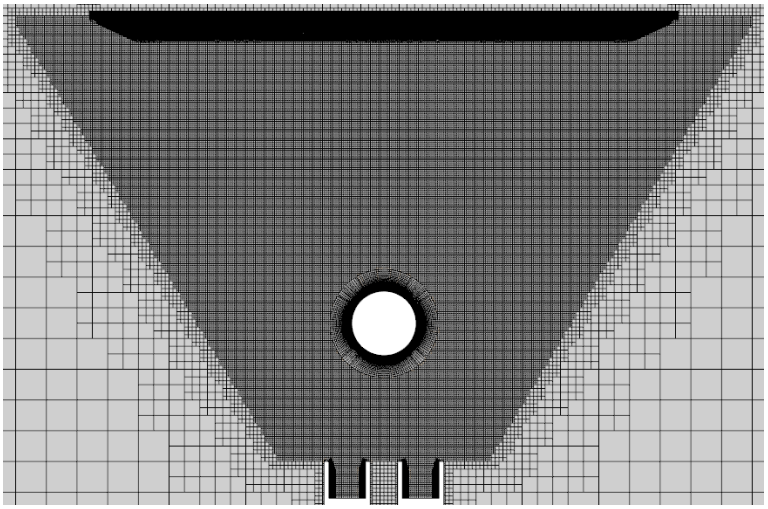

Figure 5.3: View of the x-z plane cross section of the LES mesh used to simulate DESTROJER test facility and flow obstacle.

5.4 Solution Methods

5.4.1 Jet Inlet Conditions

The jet inlet conditions used for the STRUCT-ε simulations is the same as described in Section 4.5.1. The use of a steady state pipe segment simulation was used to determine the LES jet inlet conditions, but different boundary condition parameters are used for LES. The velocity, turbulence intensity, and turbulent length scale (Equation 4.1)

Mesh Details		
Fluid Domain	Base Size	21.2mm
Cylindrical Obstacle (refinement zone)	# of Prism Layers	65
	Prism Layer Near Wall Thickness	0.005mm
	Prism Layer Total Thickness	15mm
	Mesh Refinement	6.25%
Cylindrical Obstacle (unrefined)	# of Prism Layers	15
	Prism Layer Near Wall Thickness	0.005mm
	Prism Layer Total Thickness	4.5mm
	Mesh Refinement	12.5%
Impingement Plate	# of Prism Layers	37
	Prism Layer Near Wall Thickness	0.05mm
	Prism Layer Total Thickness	16mm
	Mesh Refinement	6.25%
Jets	# of Prism Layers	56
	Prism Layer Near Wall Thickness	0.005mm
	Prism Layer Total Thickness	4.5mm
	Mesh Refinement	6.25%
Outlets	# of Prism Layers	21
	Prism Layer Near Wall Thickness	0.05mm
	Prism Layer Total Thickness	3.5mm
	Target Surface Size	6.25%

Table 5.1: Meshing details for the LES DESTROJER simulations, percents represent percentage of the base mesh size.

profiles are extracted and used as the inlet conditions. Turbulence intensity

$$I = \sqrt{\frac{2}{3}k} \; / \; \overline{U} \tag{5.1}$$

where $\overline{U}$ is the mean velocity, is a measure of the level of turbulence present [34].

5.4.2 Simulation Implementation

The STRUCT-ε model was implemented as described in Section 4.5.2. The LES simulation was implemented using the WALE subgrid scale model. A complete description of the WALE subgrid scale method can be seen in Appendix A.4.1.

The LES solutions were conducted in two stages in the same manner as the STRUCT-ε model. The first stage was a 25,000 iteration steady stage to initialize flow conditions before starting the transient stage where all data collection occurred.

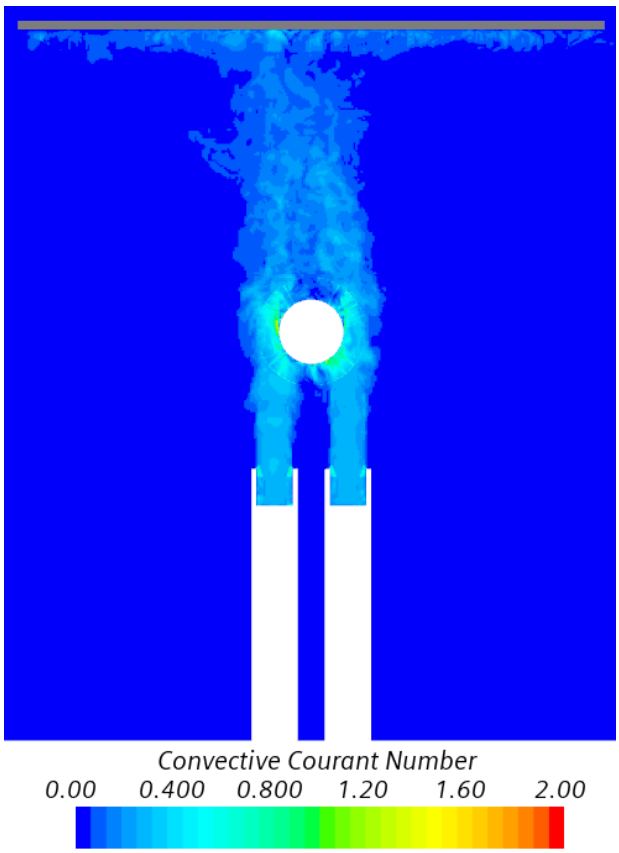

Figure 5.4: Courant number of LES on the x-z plane with a time step of $1 * 10^{-5}$.

The transient stage was completed with a time step of $5 * 10^{-5}$, a total run time of 30.0s, and data collection for FFt and RMS of temperature occurring between 10.0 and 30.0s. Data collection for POD analysis occurs every 1.0ms between 20.0 and 30.0s due to POD analysis's higher computational demand and to maintain the same 10.0s analysis window used in the STRUCT-ε simulations. The time step was selected so that the Courant number was approximately 1.0 throughout the fluid domain as seen in Figure 5.4.

LES is ran for only 30.0s due to the much higher computational demand of the simulations. A total run time of 30.0s with data collection beginning at 10.0s was found to be sufficient for flow behavior convergence as seen in Figure 5.5.

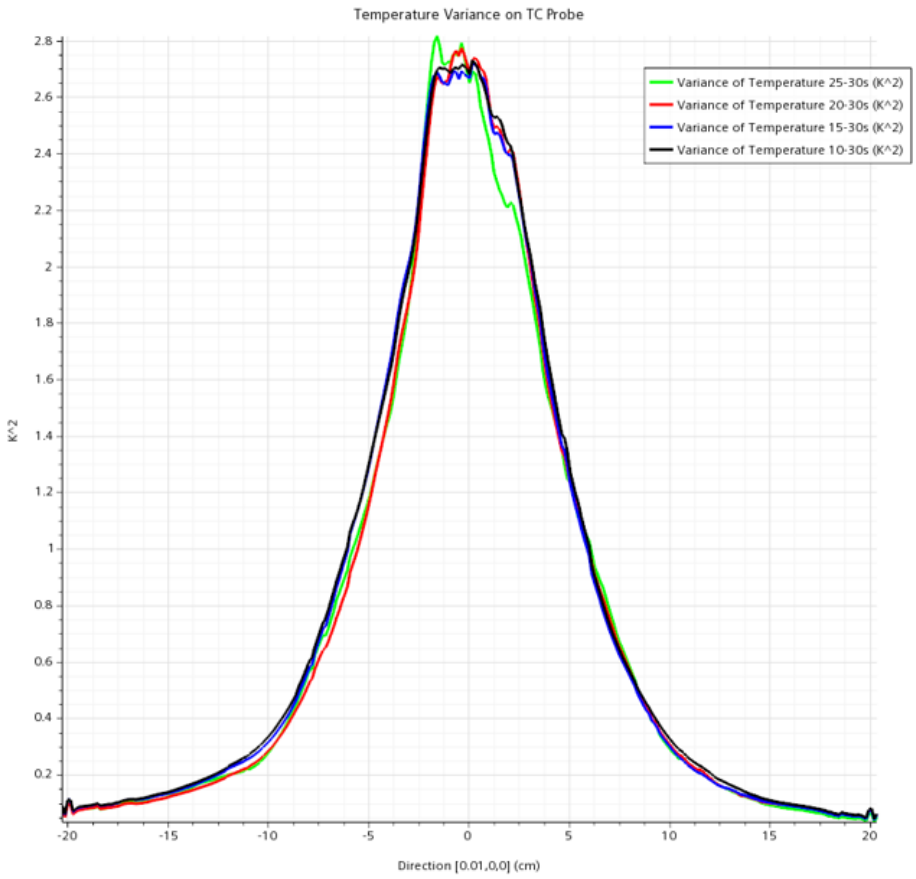

Figure 5.5: Variance of temperature measured along the axis of the TC probe in different time windows.

5.5 Results and Discussion

5.5.1 1.75D Obstacle

The average velocity in the z direction for the STRUCT-ε and LES results are shown in Figure 5.6. Both STRUCT-ε and LES have some visible downwash in the area around the obstacle, but both models have a large area of jet interference and mixing between the obstacle and impingement plate. This area of jet interference was not present in the results presented in Section 4.7.1 and demonstrates that a cylindrical obstacle is a viable option for inducing thermal striping behavior in the DESTROJER test facility. The STRUCT-ε model also displays an earlier flow separation from the obstacle than that seen in the LES solution, a feature likely to have a large influence on the differences between the predictions of the two models.

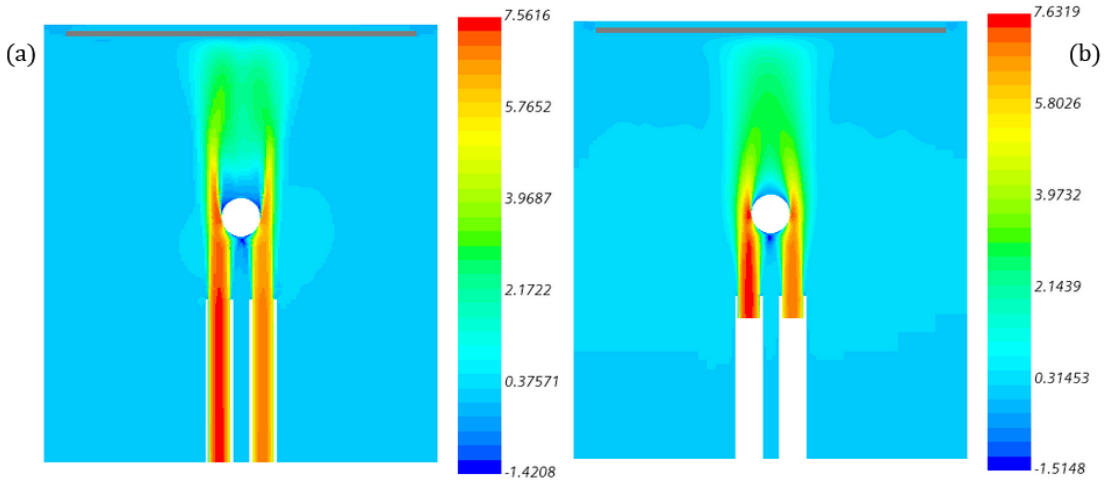

Figure 5.6: Average velocity in the z direction seen on the x-z plane beneath the impingement plate from (a) STRUCT-ε and (b) LES with 1.75D obstacle.

A closer look at the average velocity in the z direction can be seen in Figure 5.7. The mean velocity in the z direction is plotted in the y-z plane at z positions of 2D above the center of the obstacle, 0.25D below the impingement plate, and at a z position at the midpoint of the two previously described lines. In comparison to LES, STRUCT-ε is shown to consistently predict lower average velocities at the center line between the two jets and higher average velocities outside the area of jet interference. The higher velocities seen outside the area of jet interference are likely a

result of STRUCT-ε underestimating the extent of the interference between the jets which causes a smaller portion of the flow to be diverted from the z direction.

Turbulent Structure Size

The most significant difference between the two models is that the STRCUT-ε model maintains distinct jets further past the obstacle than the LES model as an effect of the different flow separations predicted. The greater survival of the jets implies that STRUCT-ε under-predicts the dissipation of large turbulent structures into smaller eddies. Figure 5.8 provides a view of the magnitude of velocity in the final time step of the LES and STRUCT-ε simulations while Figure 5.9 displays the Q-Criterion iso-surface of 250 s^{-2}. The STRUCT-ε model captures the turbulent structures produced from flow past the obstacle and jet interference, but is unable to produce the smaller turbulent structures visible in LES. These results align with the expected behavior of the STRUCT-ε model which was designed to resolve large scale structures which dissipate slower in the absence of interaction with smaller scale turbulent structures [10].

Temperature Variance

The difference in turbulent structure resolution between STRUCT-ε and LES affects the location and magnitude of temperature variance along the impingement plate as seen in Figure 5.10. In LES, mixing between the jets occurs in a larger area beneath the obstacle and most of the variance occurs just past the obstacle. In the STRUCT-ε model results, the primary location of mixing and temperature variance occurs after the obstacle and near to the impingement plate. The greater intensity of interference near to the impingement plate is also visible in Figure 5.11. The STRUCT-ε model produces a maximum RMS of temperature that is nearly 3.5 times greater than that produced by LES. The area of high temperature variance in the STRUCT-ε results is also more concentrated likely because of the continued under-prediction of mixing and turbulent structure dissipation.

A closer look at the RMS of temperature measured along the optical fiber location,

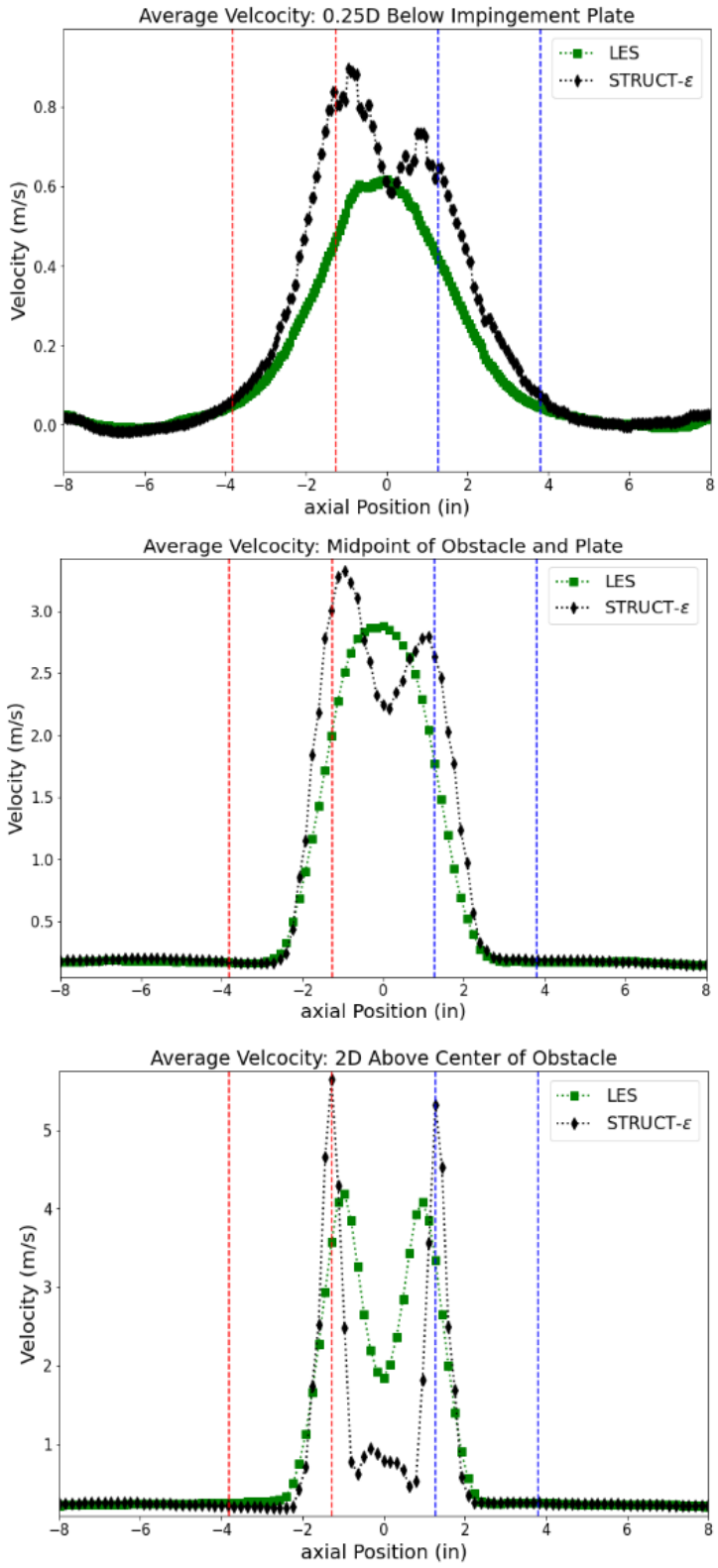

Figure 5.7: Average velocity in the z direction plotted at $0.25D$ below the impingement plate, $2D$ above the center of the obstacle, and the midpoint between those two locations for the $1.75D$ obstacle case.

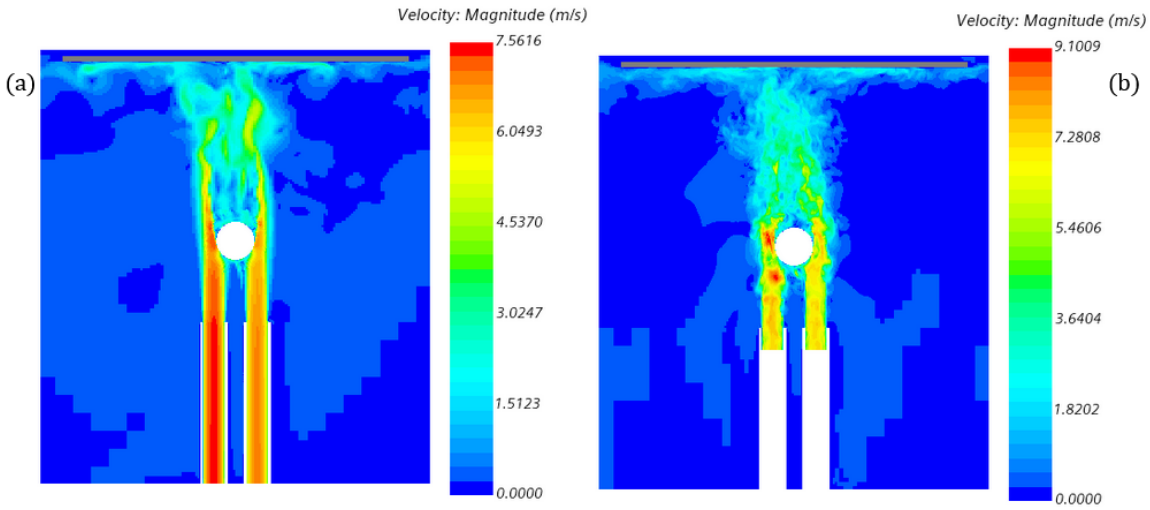

Figure 5.8: Snapshot of the magnitude of velocity on the x-z plane under the impingement plate from (a) STRUCT-ε and (b) LES with $1.75D$ obstacle.

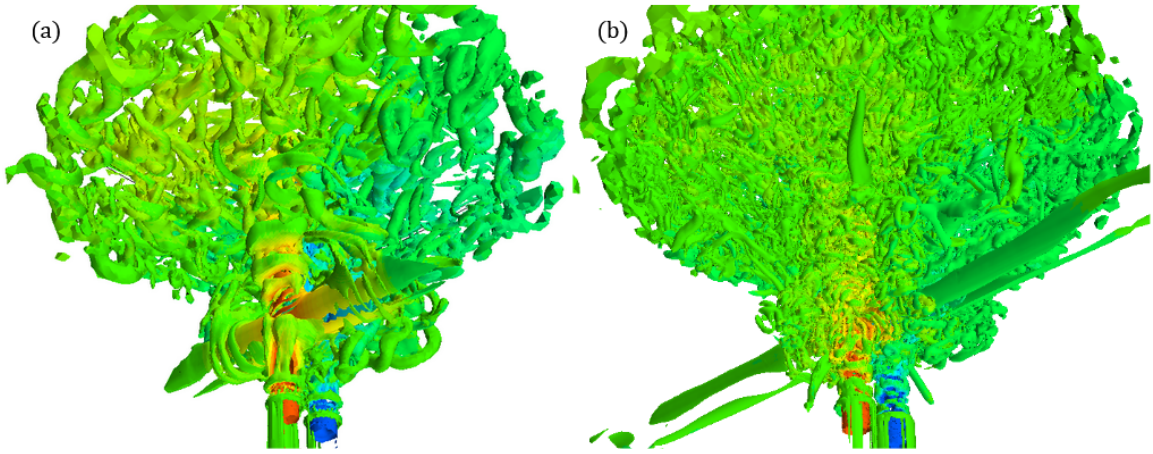

Figure 5.9: Temperature of the fluid displayed on a Q-Criterion = 250 $/s^2$ iso-surface from (a) STRUCT-ε and (b) LES with $1.75D$ obstacle.

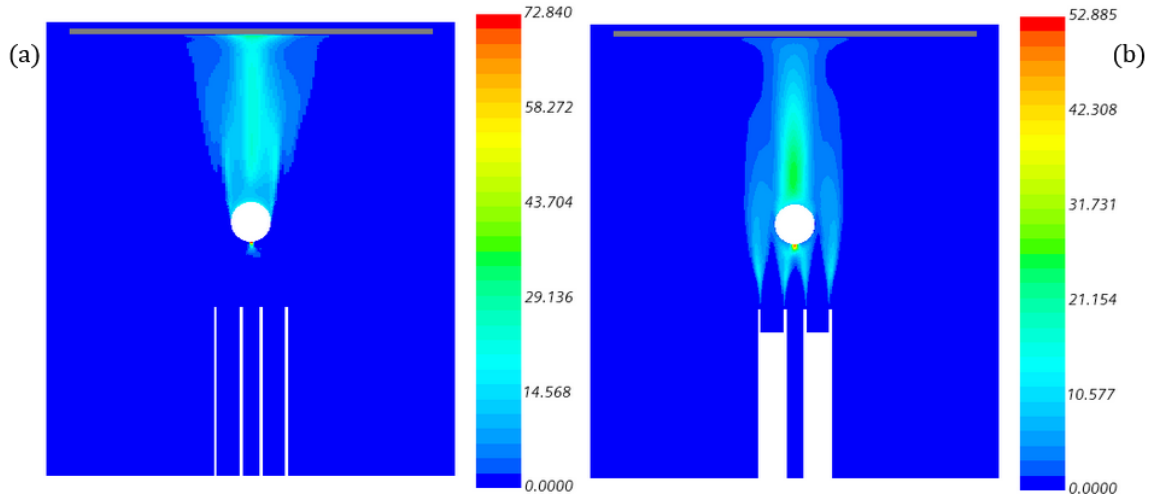

Figure 5.10: Variance of temperature displayed on the x-z plane under the impingement plate from (a) STRUCT-ε and (b) LES with $1.75D$ obstacle.

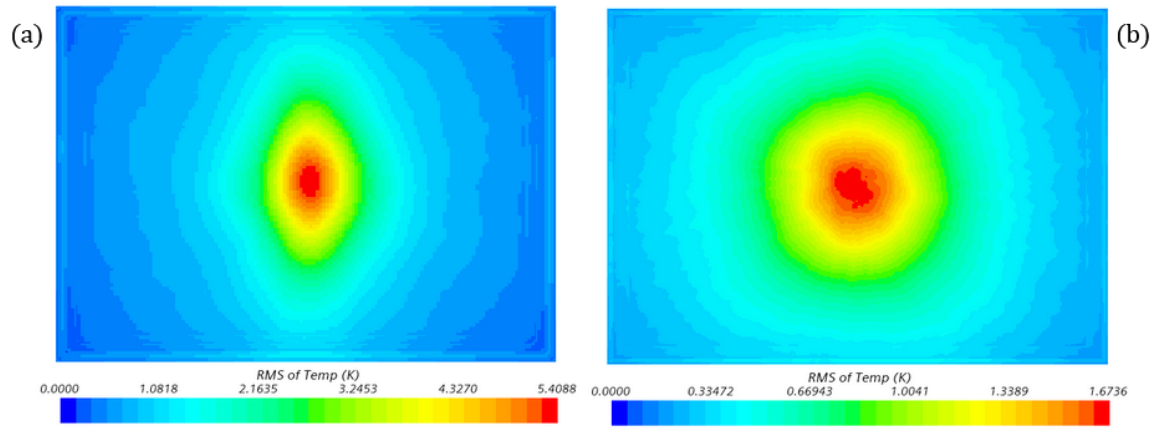

Figure 5.11: Variance of temperature measured on the TC plane from (a) STRUCT-ε and (b) LES with $1.75D$ obstacle.

where experimental results would be measured, is visible in Figure 5.12. Along the optical fiber the increased RMS of temperature seen in the STRUCT-ε results is even more pronounced. While STRUCT-ε under-predicts mixing, this leads to over-prediction of temperature variance. Therefore STRUCT-ε has the potential for use in the prediction of the presence of thermal striping as it provides a conservative estimate.

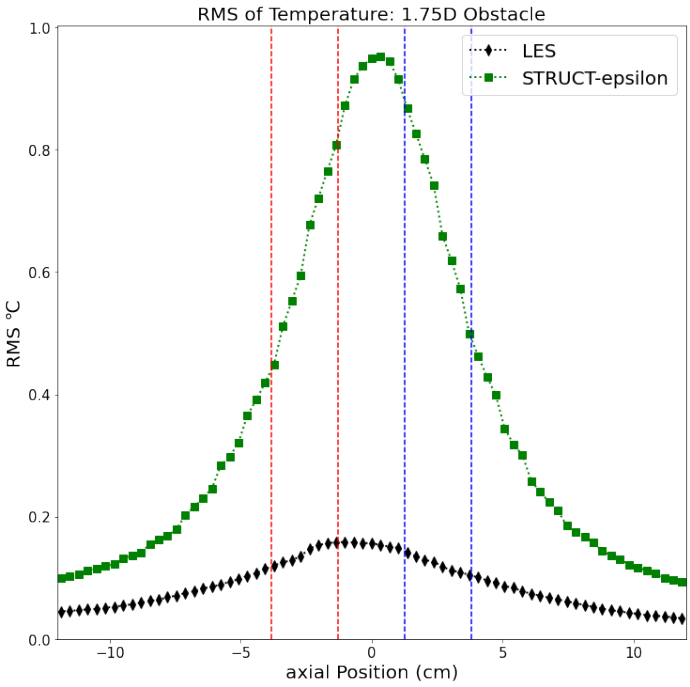

Figure 5.12: Comparison of the RMS of temperature from STRUCT-ε and LES measured along the optical fiber.

POD Analysis

POD analysis is performed in the region, pictured in Figure 5.13, is defined by the x-z plane bound by the impingement plate and $1.375D$ above the top of the cylindrical obstacle and by $3.5D$ left and right of the center of the obstacle in the x direction. Additionally, the POD analysis performed on the LES results is conducted on every other grid cell. This smaller POD analysis region and decreased spatial resolution for LES is done due to the high computational demand needed for the POD analysis calculations.

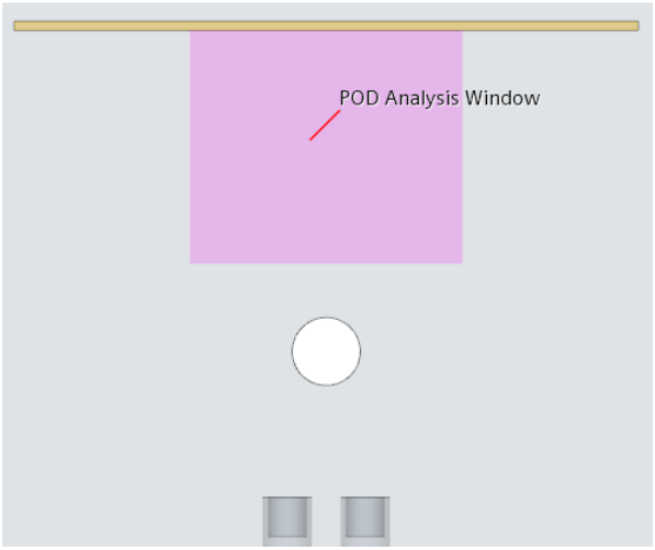

Figure 5.13: Region used for LES and STRUCT-ε comparison POD analysis.

Results of the first POD mode analysis are shown in Figure 5.14. The presence of flow oscillation is visible in both the LES and STRUCT-ε solutions. The oscillation in STRUCT-ε spans the complete length of the analysis zone which aligns with the jets greater survivability of the jets. Two distinct areas of oscillation are seen in the LES POD analysis: one narrow region near the obstacle and a broader region near to the impingement plate. The distinct oscillation area near the obstacle is likely partially responsible for the more complete mixing seen in LES. Both LES and STRUCT-ε are seen to have a distinct temperature oscillation centered between the jets, but the LES result's highest intensity is near the obstacle while the STRUCT-ε has the greatest intensity near the impingement plate.

The frequency of these oscillations are displayed in Figure 5.15. STRUCT-ε has a peak frequency of 0.7 Hz while LES has a peak frequency around 1.0 Hz. These frequencies are on the lower end of the range of interest for thermal striping behavior. The $1.75D$ obstacle was able to induce strong, distinct oscillations between the two jets while main, but the ideal frequencies for thermal striping were not achieved.

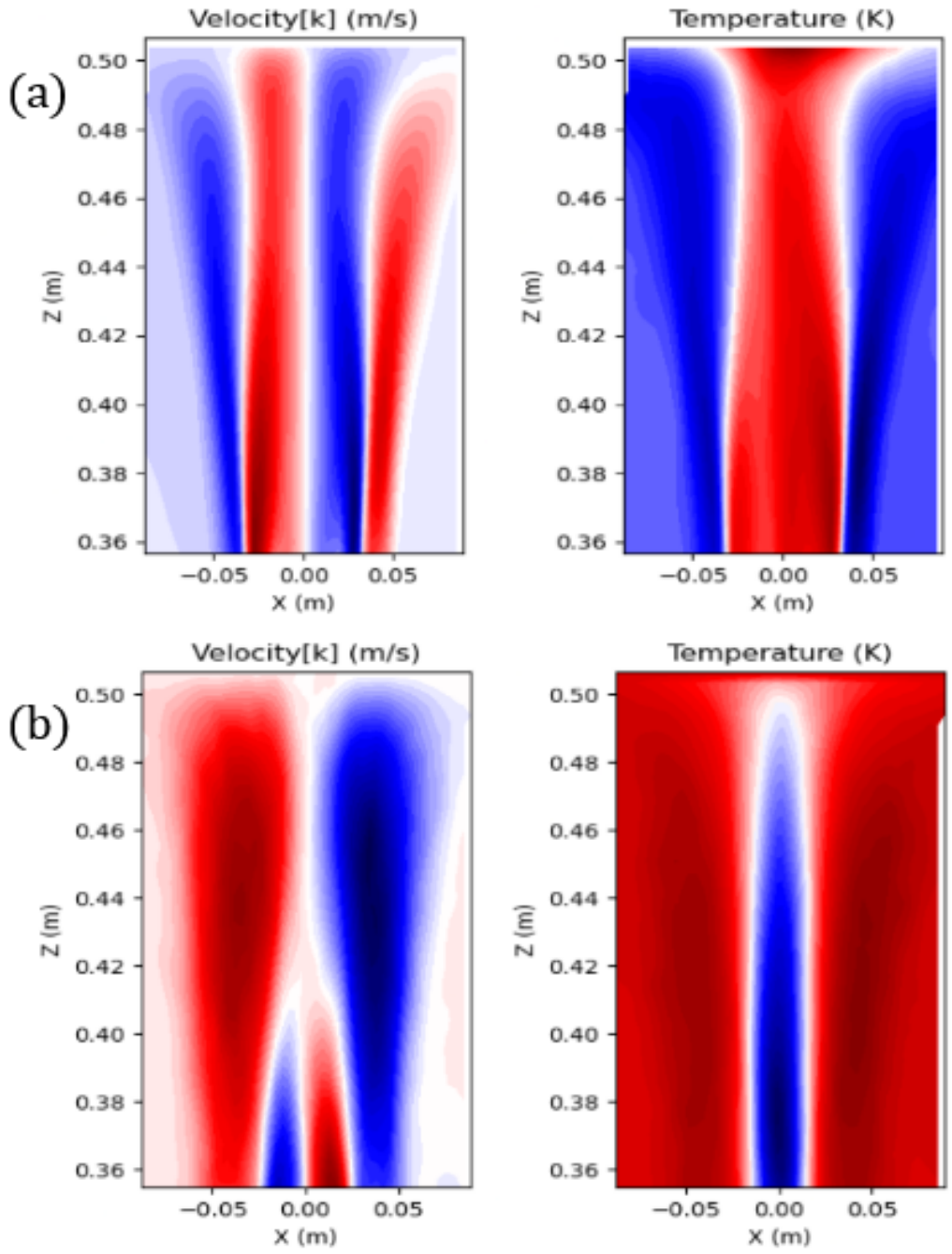

Figure 5.14: First POD mode of z velocity and temperature on the x-z plane between the impingement plate and $1.375D$ above the top of the cylindrical obstacle from (a) STRUCT-ε and (b) LES.

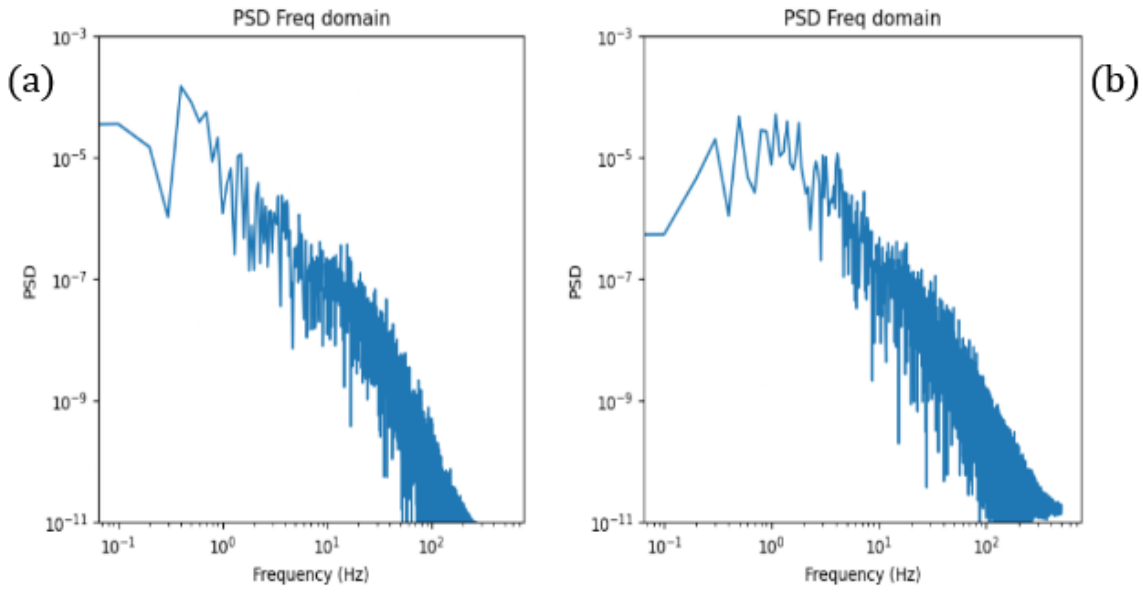

Figure 5.15: PSD frequency domain of first POD mode from (a) STRUCT-ε and (b) LES.

5.5.2 3.5D Obstacle

The average velocity in the z direction for the $3.5D$ obstacle LES and STRUCT-ε solutions is presented in Figure 5.16. Both LES and the STRUCT-ε models capture a downwash at the bottom of the obstacle. The LES results are similar to those seen in Section 5.5.1, but the jets wrap around the obstacle more tightly and the area of mixing appears smaller. The STRUCT-ε model similarly shows the jets wrapping tightly around the obstacle, but also demonstrates asymmetric flow past the obstacle. The mixing occurs primarily on the hot jet side of the obstacle as opposed to centered as seen in LES.

A view of the magnitude of velocity in the final time step of the STRUCT-ε and LES simulation is seen in Figure 5.17. In the STRUCT-ε case the cold jet fluid is seen to wrap around the cylinder obstacle while the hot jet experiences flow separation. The jets then mix at a 45 degree angle from the jet center-line, largely failing to impinge at the impingement plate. The LES case also shows that the jets experience earlier flow separation than in the $1.75D$ obstacle case. The flow quickly becomes diffuse and little mixing is demonstrated. Future studies should investigate

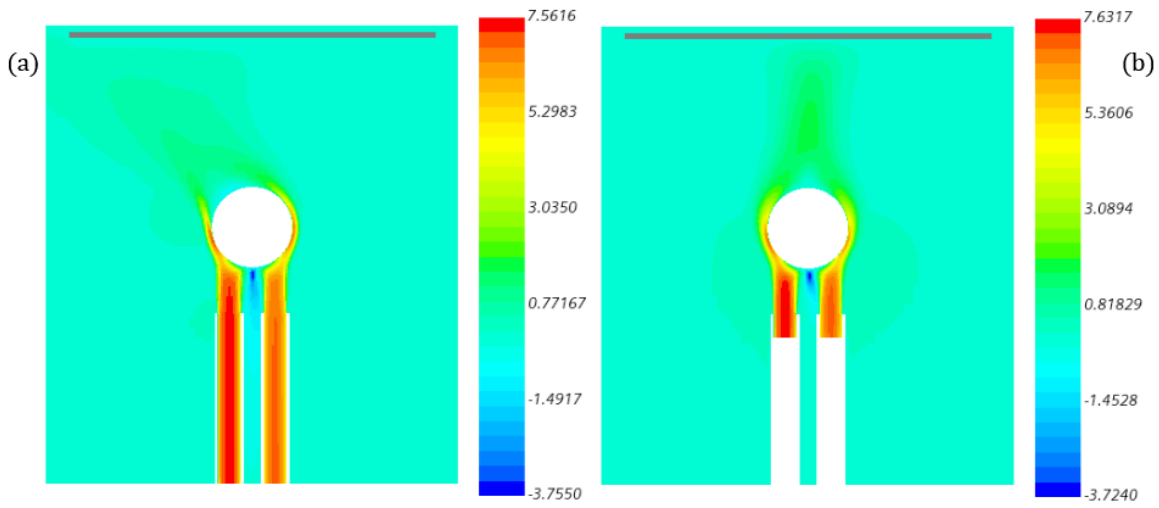

Figure 5.16: Average velocity in the z direction seen on the x-z plane beneath the impingement plate from (a) STRUCT-ε and (b) LES with 3.5D obstacle.

the impact that improved inlet condition treatments have on prediction accuracy for the STRUCT-ε model.

The off axis mixing of the jets in the STRUCT-ε case greatly effects the average velocity in the z direction as demonstrated in Figure 5.18. At 2D above the center of the obstacle LES and STRUCT-ε predict similar results. The primary difference between the two predictions being that the STRUCT-ε velocity profile is slightly shifted towards the hot jet. At the middle line the STRUCT-ε velocity profile is further shifted from the LES velocity profile in the direction of the hot jet and the magnitudes predicted are smaller as the flow does not primarily travel in the z direction. By the time the flow has reached the impingement plate the mean velocity profiles predicted by LES and STRUCT-ε have completely diverged from each other.

The dramatic difference in the predictions may be stem from the fact that the STRUCT-ε model produces fewer, larger turbulent structures than the LES simulation as seen from the Q-Criterion isosurface of 250 s^{-2} shown in Figure 5.19. The decreased dissipation of turbulent structures could be one explanation for the asymmetric flow past the obstacle. The increased stability from the lack of turbulent dissipation increases the amount of time needed for flow separation from the obstacle wall to occur.

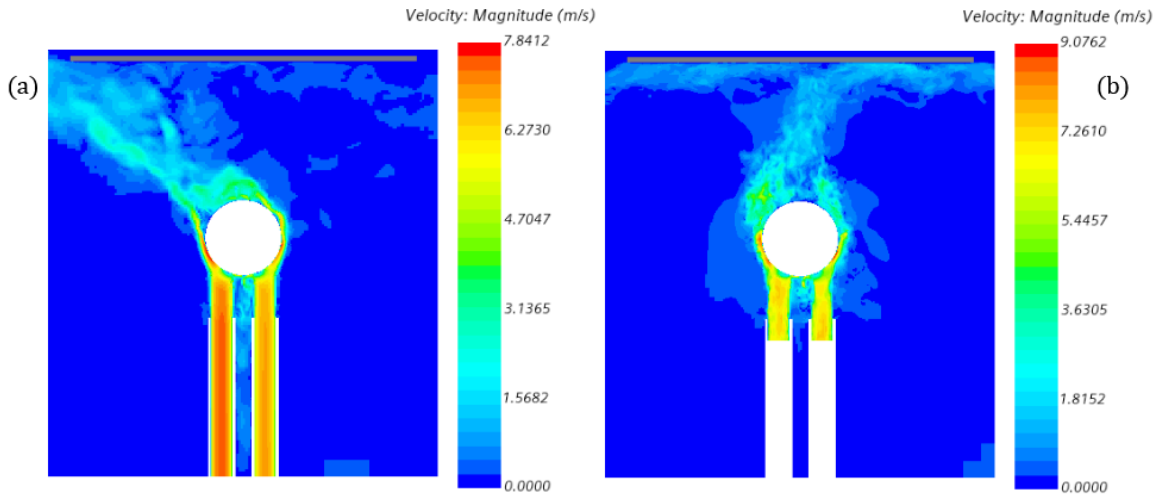

Figure 5.17: Snapshot of the magnitude of velocity on the x-z plane under the impingement plate from (a) STRUCT-ε and (b) LES with 3.5D obstacle.

Temperature Variance

The temperature variance seen in Figure 5.20 is much weaker than that seen in the 1.75D obstacle case. In the LES simulation most of the temperature variance occurs along the obstacle surface or just after the obstacle with no significant variance happening at the impingement plate. The STRUCT-ε model simulation produces the most temperature variance in the area directly after the obstacle where the hot and cold jet combine. No significant temperature variance is seen near the impingement plate.

It can also be seen in both Figure 5.10 and Figure 5.20 that LES predicts higher variances than STRUCT-ε before the jets reach the obstacle. This then correlates to higher turbulent energy at the obstacle boundary layer in the LES solution. The LES boundary layer thus remains attached longer in both cases, with the difference being especially apparent in the 3.5D obstacle case. The difference could stem from the fact that the two models resolve the boundary layer to different extents due to the different meshes used. However, the LES simulation also utilizes an unsteady inlet condition with synthetic turbulence which contributes to the generation of high variance earlier in the flow. STRUCT-ε, on the other hand, utilizes a simpler steady

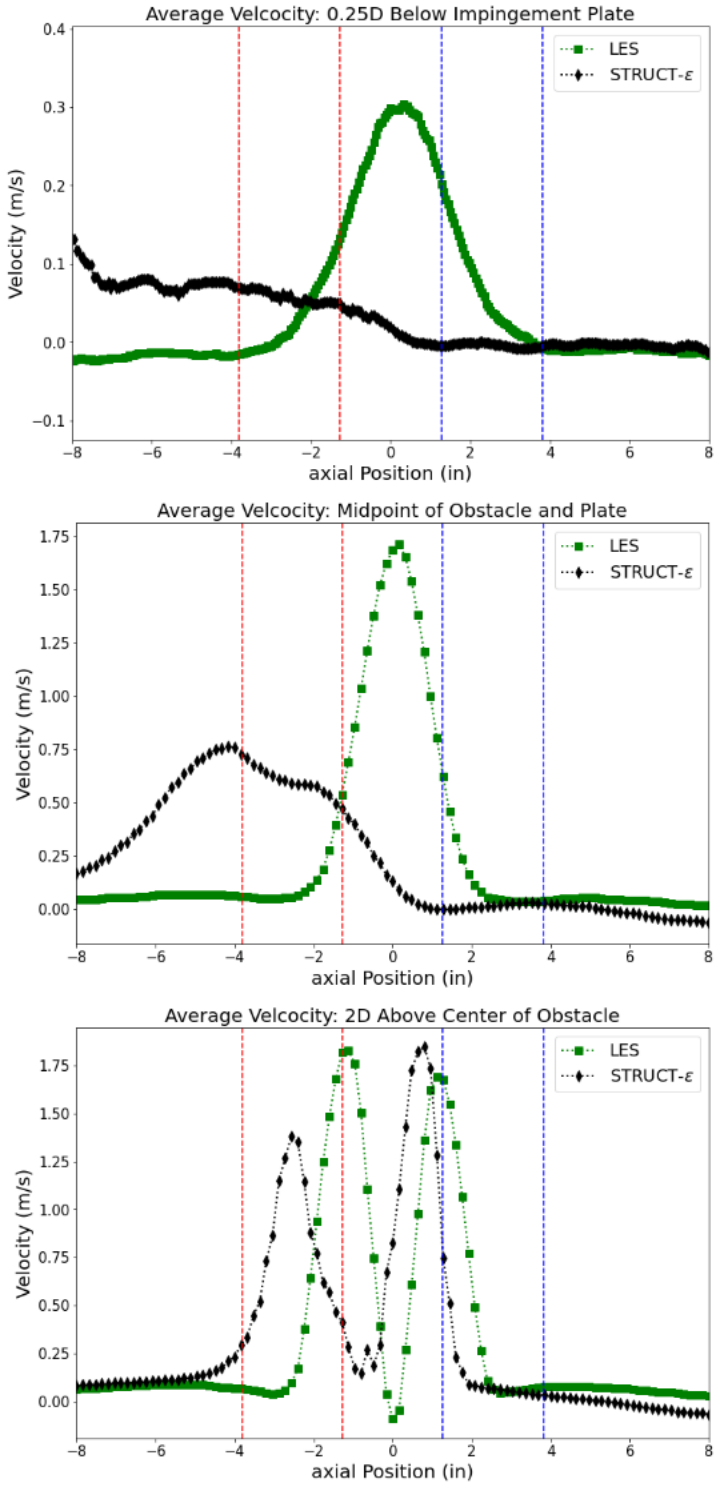

Figure 5.18: Average velocity in the z direction plotted at $0.25D$ below the impingement plate, $2D$ above the center of the obstacle, and the midpoint between those two locations for the $3.5D$ obstacle case.

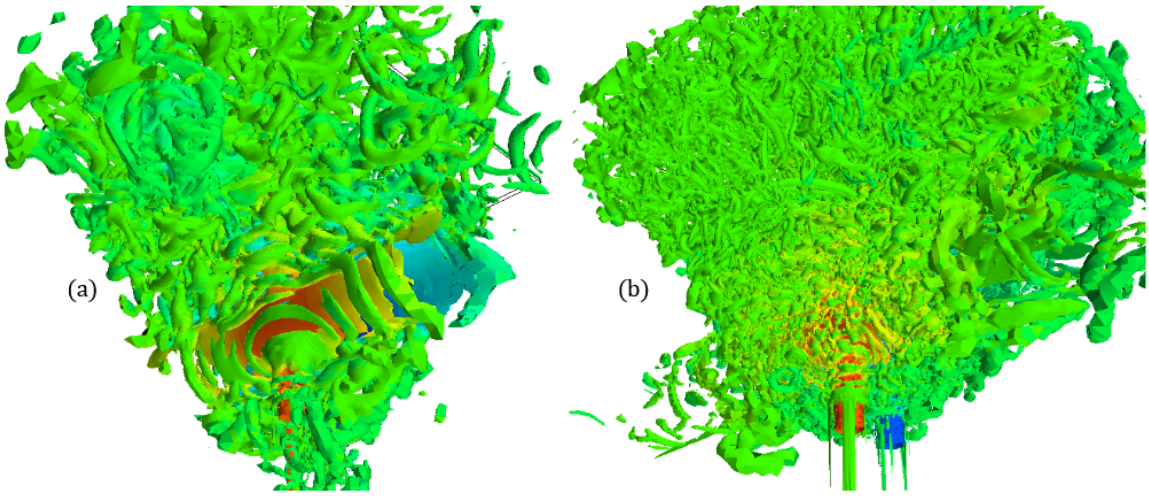

Figure 5.19: Temperature of the fluid displayed on a Q-Criterion $= 250\ /s^2$ iso-surface from (a) STRUCT-ε and (b) LES with $3.5D$ obstacle.

inlet condition that saves on computation complexity, but does not generate the early flow variance correctly. This difference appears to be the largest contributor to the difference between the predictions of the two models.

The low amount of jet interference and mixing near the impingement plate is also visible in Figure 5.21. The magnitude of the RMS of temperature measured at the TC plane is significantly lower in the $3.5D$ case than that seen from the $1.75D$ obstacle case. The LES simulation is observed to have a larger peak RMS of temperature than the STRUCT-ε simulation. The STRUCT-ε simulation's asymmetric flow is the primary cause of this flip from the $1.75D$ obstacle case as the main flow in the STRUCT-ε simulation does not reach the impingement plate.

The RMS of temperature measured along the optical fiber, Figure 5.22, provides further insight into the decreased level of temperature variance. The STRUCT-ε model produces no substantial RMS of temperature peak due to the asymmetric flow while the LES simulation has a maximum RMS value half that seen in the $1.75D$ obstacle case. The $3.5D$ obstacle appears to be too large and causes over mixing of the jets making it sub-optimal for use as an experimental configuration at the DESTROJER test facility.

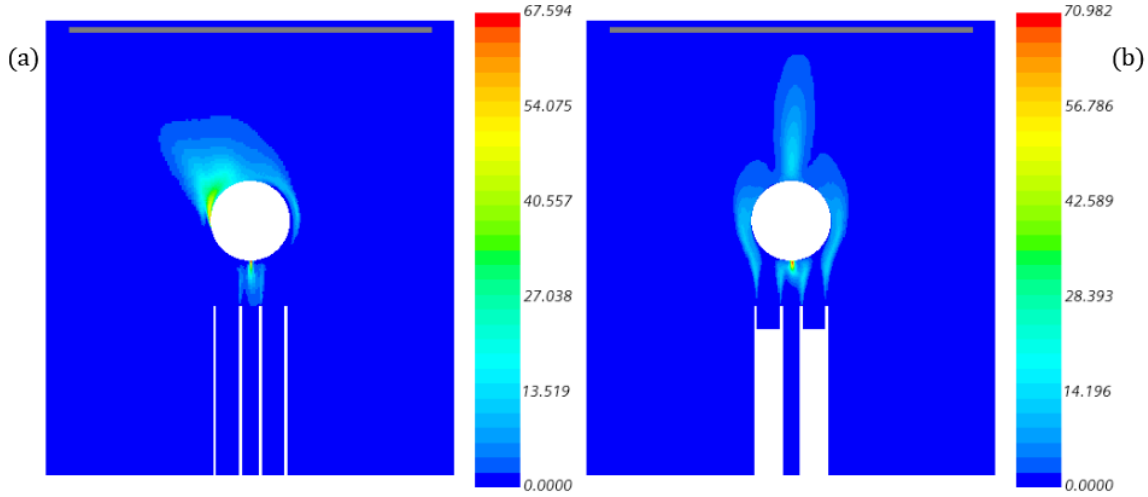

Figure 5.20: Variance of temperature displayed on the x-z plane under the impingement plate from (a) STRUCT-ε and (b) LES with $3.5D$ obstacle.

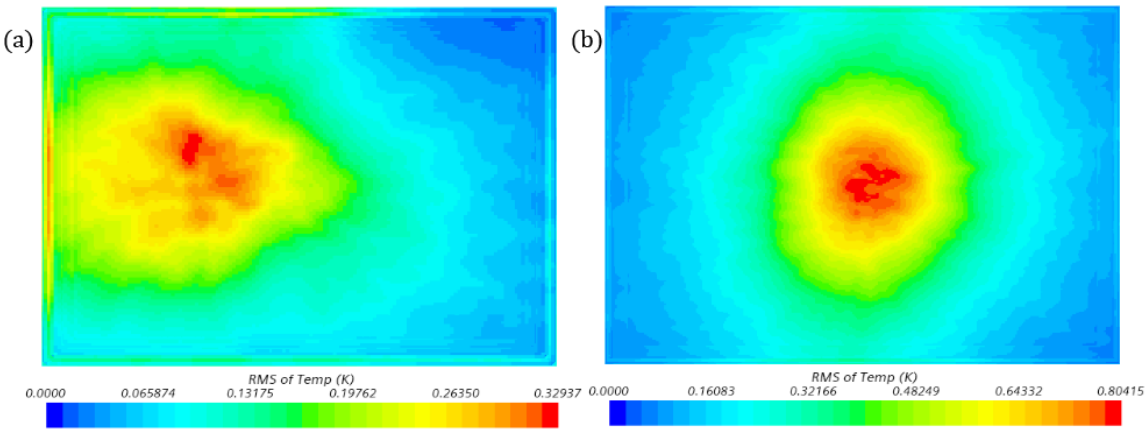

Figure 5.21: Variance of temperature measured on the TC plane from (a) STRUCT-ε and (b) LES with $3.5D$ obstacle.

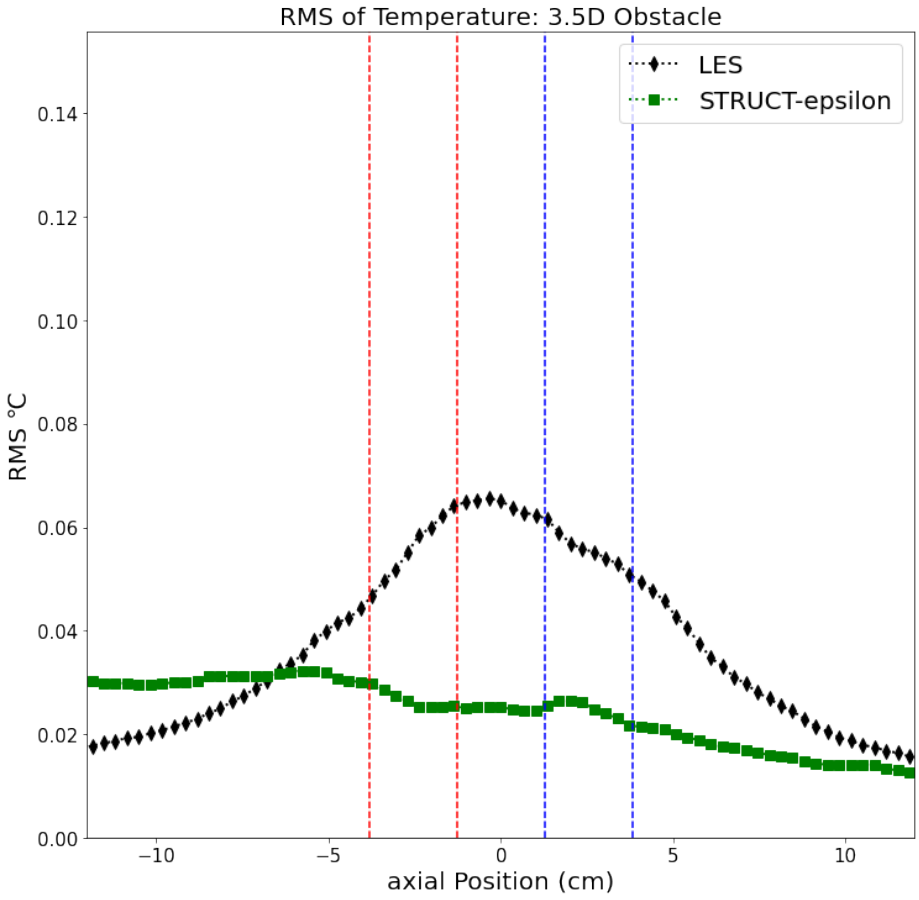

Figure 5.22: Comparison of the RMS of temperature from STRUCT-ε and LES simulations measured along the optical fiber.

POD Analysis

The POD analysis is performed on the same region shown in Figure 5.13 and in the same manner used in the $1.75D$ obstacle case. The first mode POD analysis results are shown in Figure 5.23 for the LES simulation. POD analysis was not performed on the STRUCT-ε results as the primary flow behavior is outside of the POD analysis zone. The POD analysis results are quite similar to the LES POD results seen in the $1.75D$ obstacle case, but the oscillating region does not extend the full way to the impingement plate. The jets have fully mixed by the time they reach the impingement plate and thus no oscillation region exists at the plate. The z velocity and temperature oscillation regions have a peak frequency of approximately 5 Hz which is within the 1 to 10 Hz range that corresponds with the most damaging thermal striping behavior.

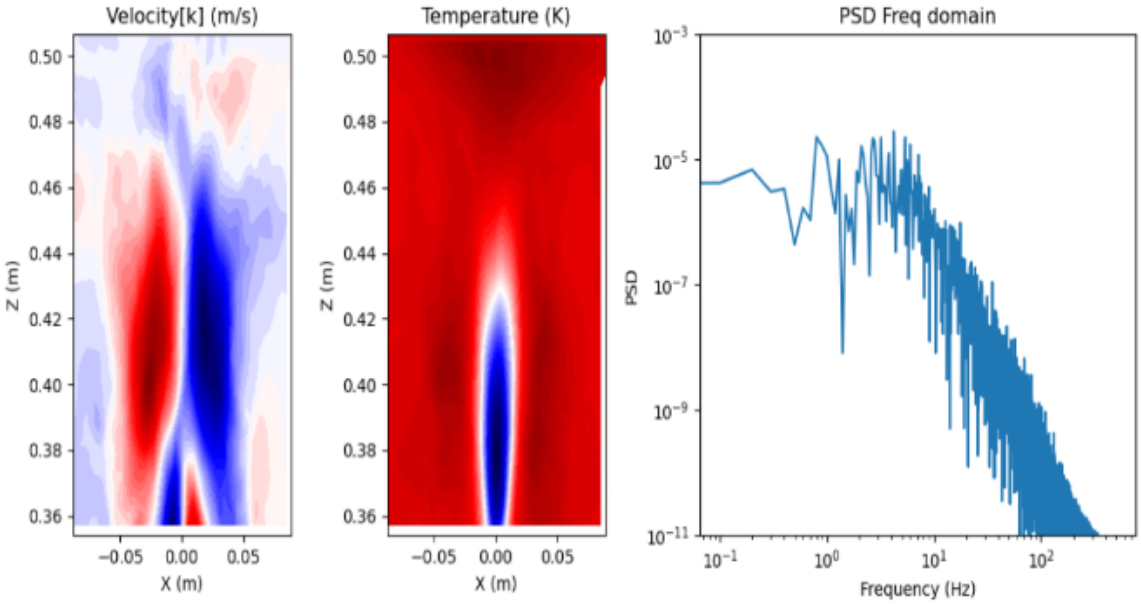

Figure 5.23: First LES POD mode of the z Velocity and temperature along with the PSD frequency domain calculated on the x-z plane between the impingement plate and $0.5D$ above the top of the cylindrical obstacle.

The $3.5D$ cylindrical obstacle with a $12D$ raised impingement plate case is not a promising candidate for use at the DESTROJER test facility. The low temperature variance at the impingement plate does not allow for sufficient thermal striping. The 5 Hz frequency seen in the POD analysis of the LES simulation is promising though

and future work should investigate repositioning the impingement plate to increase the temperature variance while mainting the oscillatory frequency.

While the $3.5D$ case is not immediately promising for use in the DESTROJER test facility, the discovery of a disagreement between the STRUCT-ε model and LES provides an important opportunity to further refine the STRUCT-ε model.

Chapter 6

Conclusion

The intent of this work was to develop experimental test cases for the study to be conducted at the DESTROJER test facility while also examining the validity of the STRUCT-ε model in novel flow cases. The use of the STRUCT-ε model enabled the study of multiple different experimental configurations in one fifth of the time needed for comparable LES solutions.

The use of a flow obstructing cylindrical obstacle proved effective in inducing oscillatory mixing. While the STRUCT-ε and LES results showed significant differences in the magnitude of the induced oscillations, STRUCT-ε was able to successfully predict the the stable oscillatory flow behavior of the $1.75D$ obstacle configuration and the distorted flow seen in the $3.5D$ obstacle configuration. Continued investigation of the optimal size and placement of the cylindrical obstacle should be conducted to find the configuration that best induces the sought after thermal striping behavior in the DESTROJER test facility. Future implementation of the experiment will allow for the evaluation of STRUCT-ε's performance against experimental results and enable a better understanding of the model's limitations.

The findings explored in this work present new opportunities in the development of the STRUCT-ε model. Future work on validating STRUCT-ε should evaluate the model's performance in known asymmetric and complex flow cases. Special attention should also be placed on analyzing the impact of differences between the LES and STRUCT-ε runs, such as the method used for inlet conditions. Developing a deeper

understanding of and refining the STRUCT-ε model is necessary for its implementation as predictive safety tool in nuclear reactor design.

Bibliography

[1] Jacopo Buongiorno, John Parsons, Michael Corradini, and David Petti. The Future of Nuclear Energy in a Carbon-Constrained World. Technical report, Massachusetts Institute of Technology, 2018.

[2] World Nuclear Association. How can nuclear combat climate change, 2022.

[3] The GEN IV International Forum. Generation IV Systems, 2022.

[4] IAEA. Operational & Long-Term Shutdown Reactors. Power Reactor Information System, April 2022.

[5] Ian Jones. The Thermal Striping Project. Technical report, Liverpool John Moores University, 2013.

[6] Tomasz Bury. Coupling of CFD and lumped parameter codes for thermal-hydraulic simulations of reactor containment. *Computer Assisted Methods in Engineering and Science*, 20:195–206, 2013.

[7] Emilio Baglietto, Ralph Wiser, Elia Merzari, Victor Petrov, Annalisa Manera, Wayne Strasser, Dillon Shaver, Hangbok Choi, Mathieu Martin, and Dustin Langewisch. Challenge Problem 2: Benchmark Specifications for Thermal Striping of Reactor Internals. Technical report, Argonne National Laboratory, Mar 2021.

[8] Jinyong Feng, Liangyu Xu, and Emilio Baglietto. Assessing the Applicability of the Structure-Based Turbulence Resolution Approach to Nuclear Safety-Related Issues. *Fluids*, 6, 2021.

[9] William L. Oberkampf and Matthew F. Barone. Measures of agreement between computation and experiment: Validation metrics. *Journal of Computational Physics*, 217:5–36, 2006.

[10] Ka-Yen K. Yau. Application of Hybrid CFD Turbulence Model, STRUCT-ϵ, on Heated Flow Cases. Masters Thesis, Massachusetts Institute of Technology, 2019.

[11] Monica Pham, Emilio Baglietto, Victor Petrov, and Annalisa Manera. Assessing the Structure-Based Turbulence Model Performance with Symmetrical Jet Experiments. In *Proceedings of Advances in Thermal Hydraulics*, pages 262–273, Anaheim, California, 2022.

[12] Yue Jin, Jinyong Feng, Emilio Baglietto, and Koroush Shirvan. Numerical Investigation of the Turbulent Mixing and Thermal Striping Phenomena in the General Atomics HTGR Upper Plenum. Technical report, Massachusetts Institute of Technology, 2022.

[13] Brendan Vaughan. *Design of a Thermal Striping Experiment Aided by Hybrid CFD Turbulence Model, STRUCT-ϵ*. Undergrad thesis, Massachusetts Institute of Technology, 2023.

[14] Joel H. Ferziger and Milovan Peric. *Computational Methods for Fluid Dynamics*. Springer-Verlag Berlin Heidelberg, 2002.

[15] Stephen B. Pope. *Turbulent Flows*. Cambridge University Press, 2013.

[16] Emilio Baglietto. Lecture 11: Turbulence and Turbulence Modeling. Applied Computational Fluid Dynamics and Heat Transfer, March 2023.

[17] Paul A. Durbin and Bjørn A. Pettersson-Reif. *Statistical Theory and Modeling for Turbulent Flow*. Wiley, 2011.

[18] Daniel Nunez. *High-Resolution Experiments of Momentum- and Buoyancy-Driven Flows for the Validation and Advancement of Computational Fluid Dynamics Codes*. PhD thesis, University of Michigan, 2020.

[19] Parviz Moin and Krishnan Mahesh. Direct Numerical Simulation: A Tool in Turbulence Research. *Annual Review of Fluid Mechanics*, 30:539–578, 1998.

[20] Emilio Baglietto. Lecture 15: RANS and RSM. Applied Computational Fluid Dynamics and Heat Transfer, April 2023.

[21] Emilio Baglietto and Hisashi Ninokata. Improved Turbulence Modeling for Performance Evaluation of Novel Fuel Designs. *Nuclear Technology*, 158:2:237–248, May 2007.

[22] Jinyong Feng, Emilio Baglietto, Koichi Tanimoto, and Yoshiyuki Kondo. Demonstration of the STRUCT turbulence model for mesh consistent resolution of unsteady thermal mixing in a T-junction. *Nuclear Engineering and Design*, 361:237–248, May 2020.

[23] Franck Nicoud and Frédéric Ducros. Subgrid-scale stress modelling based on the square of the velocity gradient tensor. *Flow, Turbulence and Combustion*, 62, 1999.

[24] Philippe R. Spalart. Detached-Eddy Simulation. *Annual Review of Fluid Mechanics*, 41, 2009.

[25] F. R. Menter and Y. Egorov. The Scale-Adaptive Simulation Method for Unsteady Turbulent Flow Predictions. Part 1: Theory and Model Description. *Flow, Turbulence and Combustion*, 85, June 2010.

[26] Sharath S. Girimaji, Eunhwan Jeong, and Ravi Srinivasan. Partially Averaged Navier-Stokes Method for Turbulence: Fixed Point Analysis and Comparison With Unsteady Partially Averaged Navier-Stokes. *Journal of Applied Mechanics*, 73, May 2005.

[27] Vaclav Kolar. Vortex identification: New requirements and limitations. *International Journal of Heat and Fluid Flow*, 28, May 2007.

[28] Julien Weiss. A Tutorial on the Proper Orthogonal Decomposition. *AIAA Aviation Forum*, June 2019.

[29] Robert Oshana. *DSP Software Development Techniques for Embedded and Real-Time Systems*. Newnes, 2006.

[30] Yohan Jung, Sun Rock Choi, and Jonggan Hong. Numerical analysis of temperature fluctuation characteristics associated with thermal striping phenomena in the PGSFR. *Nuclear Engineering and Technology*, 54:10:3928–3942, October 2022.

[31] McMaster-Carr. Clear Scratch- and UV-Resistant Cast Acrylic Sheet.

[32] MatWeb Matieral Property Data. Clear Scratch- and UV-Resistant Cast Acrylic Sheet.

[33] ANSYS. Introduction to ANSYS Fluent Lecture 7: Turbulence Modeling, Febrary 2012.

[34] Siemens. Simcenter STAR-CCM+: Siemens PLM Software.

[35] R. Viskanta. Heat transfer to impinging isothermal gas and flame jets. *Experimental Thermal and Fluid Science*, 6, 1993.

[36] Mohammad Jahedi. Computational study of multiple impinging jets on heat transfer. Masters Thesis, University of Gävle, 2013.

[37] L.F.G. Geers. *Multiple impinging jet arrays: an experimental study on flow and heat transfer*. PhD thesis, Delft University of Technology, 2004.

[38] Emilio Baglietto. Lecture 20: Applied LES and Hybrid-Methods. Applied Computational Fluid Dynamics and Heat Transfer, April 2023.

[39] Emilio Baglietto and Hisashi Ninokata. Anisotropic Eddy Viscosity Modeling for Application to Industrial Engineering Internal Flows. *International Journal of Transport Phenomena*, 8:2:109–125, 2006.

Appendix A

Formulations of Turbulence Models

Features of the implementations of the turbulence models discussed in chapter 2 are detailed in this appendix.

A.1 Standard k-ε Model

The transport equation for the turbulent kinetic energy in the Standard k-ε model is

$$\frac{\partial(\rho k)}{\partial t} + \frac{\partial(\rho k u_j)}{\partial x_j} = \frac{\partial}{\partial x_j}\left[\left(\mu + \frac{\mu_t}{\sigma_k}\right)\frac{\partial k}{\partial x_j}\right] - \rho\overline{u_i u_j}\frac{\partial u_i}{\partial x_j} - \rho\varepsilon \tag{A.1}$$

where μ is the dynamic viscosity and the usual value σ_k is 1. The transport equation for the turbulent dissipation is

$$\frac{\partial(\rho\varepsilon)}{\partial t} + \frac{\partial(\rho\varepsilon u_j)}{\partial x_j} = \frac{\partial}{\partial x_j}\left[\left(\mu + \frac{\mu_t}{\sigma_\varepsilon}\right)\frac{\partial \varepsilon}{\partial x_j}\right] + C_{1\varepsilon}\frac{\varepsilon}{k}\rho\overline{u_i u_j}\frac{\partial u_i}{\partial x_j} - C_{2\varepsilon}\rho\frac{\varepsilon^2}{k} \tag{A.2}$$

where $C_{1\varepsilon} = 1.44$, $C_{2\varepsilon} = 1.92$, and $\sigma_\varepsilon = 1.3$ are the standard values used. The turbulent viscosity, μ_t, is modeled as

$$\mu_t = \rho C_\mu \frac{k^2}{\varepsilon} \tag{A.3}$$

with $C_\mu = 0.09$ as the standard value. The Reynolds stresses are then calculated from the eddy viscosity assumption and found to be [17]

$$-\rho\overline{u_i u_j} = \mu_t \left(\frac{\partial U_i}{\partial x_j} + \frac{\partial U_j}{\partial x_i} \right) - \frac{2}{3}\rho k \delta_{ij} \tag{A.4}$$

A.1.1 Low-Re Approach

In the Low-Reynolds number approach, damping functions are applied to C_μ, $C_{1\varepsilon}$, and $C_{2\varepsilon}$ to modulate the coefficients as a function of the turbulence Reynolds number. The transport equations are now represented as

$$\frac{\partial}{\partial t}(\rho k) + \nabla \cdot (\rho k \overline{\boldsymbol{v}}) = \nabla \cdot \left[\left(\mu + \frac{\mu_t}{\sigma_k} \right) \nabla k \right] + P_k - \rho(\varepsilon - \varepsilon_0) + S_k \tag{A.5}$$

and

$$\frac{\partial}{\partial t}(\rho \varepsilon) + \nabla \cdot (\rho \varepsilon \overline{\boldsymbol{v}}) = \nabla \cdot \left[\left(\mu + \frac{\mu_t}{\sigma_\varepsilon} \right) \nabla \varepsilon \right] + \frac{1}{T_\varepsilon} C_{1\varepsilon} P_\varepsilon - C_{2\varepsilon} f_2 \rho \left(\frac{\varepsilon}{T_e} - \frac{\varepsilon_0}{T_0} \right) + S_\varepsilon \tag{A.6}$$

where $\overline{\boldsymbol{v}}$ is the mean velocity, the values of $C_{1\varepsilon}$, $C_{2\varepsilon}$, σ_ε, and σ_k are unchanged, and

- ε_0 is the ambient turbulence value in the source term that counteracts turbulence decay
- T_0 is the time scale of the turbulence source term defined as

$$T_0 = max\left(\frac{k_0}{\varepsilon_0}, \sqrt{\frac{\nu}{\varepsilon_0}} \right) \tag{A.7}$$

- f_2 is a damping function that is calculated as

$$f_2 = 1 - C exp\left(-Re_t^2\right) \tag{A.8}$$

  - $C = 0.3$

- Re_t is the turbulent Reynolds number

$$Re_t = \frac{k^2}{\nu\varepsilon} \tag{A.9}$$

- P_k is a production term equal to $G_k + G_b - \Upsilon_M$
  - Turbulent production $G_k = \mu_t S^2 - \frac{2}{3}\rho k \nabla \cdot \overline{\boldsymbol{v}} - \frac{2}{3}\mu_t \left(\nabla \cdot \overline{\boldsymbol{v}}\right)^2$
  - Buoyancy production $G_b = \beta \frac{\mu_t}{Pr_t}\left(\nabla \overline{T} \cdot \boldsymbol{g}\right)$
    - Coefficient of thermal expansion $\beta = -\frac{1}{\rho}\frac{\partial \rho}{\partial \overline{T}}$
    - Turbulent Prandtl number Pr_t
    - Mean temperature $\overline{T}$
    - Gravitational vector $\boldsymbol{g}$
  - Compressibility modification $\Upsilon_M = \frac{\rho C_M k \varepsilon}{c^2}$
    - $C_M = 2$
    - Speed of sound c
- P_ε is a production term equal to $G_k + +G_{nl} + G' + C_{3\varepsilon}G_b + \frac{\rho}{C_{1\varepsilon}}\Upsilon_y$
  - Nonlinear production $G_n l = (\boldsymbol{T}_{RANS,NL}) : \nabla \cdot \overline{\boldsymbol{v}}$
    - where $T_{RANS,NL}$ is the nonlinear contribution to the constitutive relationship
  - Additional production $G' = f_2\left(G_k + 2\mu\frac{k}{d^2}\right) exp\left(-ERe_d^2\right)$
    - $E = 0.00375$
  - Yap correction $\Upsilon_y = C_w \frac{\varepsilon^2}{k} max\left[\left(\frac{l}{l_\varepsilon} - 1\right)\left(\frac{l}{l_\varepsilon}\right)^2, 0\right]$
    - $C_w = 0.83$
    - $l = \frac{k^{3/2}}{\varepsilon}$
    - $l_\varepsilon = 2.55d$
  - $C_{3\varepsilon} = tanh\frac{|\boldsymbol{v}_b|}{|\boldsymbol{u}_b|}$
    - Velocity component parallel to the gravitational vector $\boldsymbol{v}_b$

* Velocity component perpendicular to the gravitational vector $\boldsymbol{u}_b$

The turbulent viscosity is now calculated as

$$\mu_t = \rho C_\mu f_\mu k T \tag{A.10}$$

where

- The damping function $f_\mu = 1 - exp\left[-\left(C_{d0}\sqrt{Re_d} + C_{d1}Re_d + C_{d2}Re_d^2\right)\right]$
  - $C_{d0} = 0.091$
  - $C_{d1} = 0.0042$
  - $C_{d2} = 0.00011$
- Turbulent time scale $T = max\left(T_e, \sqrt{\frac{\nu}{\varepsilon}}\right)$
  - Large eddy time scale $T_e = \frac{k}{\varepsilon}$

Complete details of the Standard k-ε Low-Re formulation can be found in the STAR-CCM+ Theory Guide [34].

A.2 Cubic k-ε Model

The quadratic stress strain relationship utilized in the Cubic k-ε model is

$$\begin{aligned}\rho\overline{u_i'u_j'} = {} & \frac{2}{3}\rho k\delta_{ij} - 2\mu_t S_{ij} + 4C_1\mu_t\frac{k}{\varepsilon}\left[S_{ik}S_{kj} - \frac{1}{3}\delta_{ij}S_{kl}S_{kl}\right] \\ & + 4C_2\mu_t\frac{k}{\varepsilon}\left[\Omega_{ik}S_{kj} + \Omega_{jk}S_{ki}\right] + 4C_3\mu_t\frac{k}{\varepsilon}\left[\Omega_{ik}\Omega_{kj} - \frac{1}{3}\delta_{ij}\Omega_{lk}\Omega_{kl}\right] \\ & + 8C_4\mu_t\frac{k^2}{\varepsilon^2}\left[S_{ki}\Omega_{lj} + S_{kj}\Omega_{li}\right]S_{kl} + 8C_5\mu_t\frac{k^2}{\varepsilon^2}\left[S_{kl}S_{kl} + \Omega_{kl}\Omega_{kl}\right]S_{ij}\end{aligned} \tag{A.11}$$

where

$$C_\mu = \frac{C_{a0}}{\left(C_{a1} + C_{a2}SS^3 + C_{a3}\Omega\right)C_\mu} \tag{A.12}$$

$$C_1 = \frac{C_{NL1}}{\left(C_{NL6} + C_{NL7}S^3\right)C_\mu} \tag{A.13}$$

$$C_2 = \frac{C_{NL2}}{\left(C_{NL6} + C_{NL7} S^3\right) C_\mu} \tag{A.14}$$

$$C_3 = \frac{C_{NL3}}{\left(C_{NL6} + C_{NL7} S^3\right) C_\mu} \tag{A.15}$$

$$C_4 = C_{NL4} C_\mu^2 \tag{A.16}$$

and

$$C_5 = C_{NL5} C_\mu^2 \tag{A.17}$$

The coefficients used in the quadratic stress strain relationship are found in table A.1.

C_{a0}	C_{a1}	C_{a2}	C_{a3}	C_{NL1}	C_{NL2}	C_{NL3}	C_{NL4}	C_{NL5}	C_{NL6}	C_{NL7}
0.667	3.9	1.0	0.0	0.8	11.0	4.5	-5.0	-4.5	1000.0	1.0

Table A.1: Cubic k-ε coefficients from Baglietto and Ninokata [39]

A.3 k-ω Model

The transport equations for the k-ω model are

$$\frac{\partial}{\partial t}(\rho k) + \nabla \cdot (\rho k \overline{\boldsymbol{v}}) = \nabla \cdot \left[\left(\mu + \sigma_k \mu_t\right) \nabla k\right] - \rho \beta^* \omega k + P_k \tag{A.18}$$

and

$$\frac{\partial}{\partial t}(\rho \omega) + \nabla \cdot (\rho \omega \overline{\boldsymbol{v}}) = \nabla \cdot \left[\left(\mu + \sigma_\omega \mu_t\right) \nabla \omega\right] - \rho \beta \omega^2 + P_\omega \tag{A.19}$$

where $\sigma_k = \sigma_\omega = 0.5$, $\beta^* = 0.09$, $\beta = 0.072$ and the turbulent viscosity, μ_t, is modeled as

$$\mu_t = \frac{\rho k}{\omega} \tag{A.20}$$

and

- P_k is a production term equal to $G_k + G_b$
  - Turbulent production $G_k = \mu_t S^2 - \frac{2}{3}\rho k \nabla \cdot \overline{\boldsymbol{v}} - \frac{2}{3}\mu_t \left(\nabla \cdot \overline{\boldsymbol{v}}\right)^2$
  - Buoyancy production $G_b = \beta \frac{\mu_t}{Pr_t}\left(\nabla \overline{T} \cdot \boldsymbol{g}\right)$
    - Coefficient of thermal expansion $\beta = -\frac{1}{\rho}\frac{\partial \rho}{\partial \overline{T}}$

    - Turbulent Prandtl number Pr_t
    - Mean temperature $\overline{T}$
    - Gravitational vector $\boldsymbol{g}$

- P_ω is a production term equal to G_ω
  - Specific dissipation production $G_\omega = \rho\alpha\left[\left(S^2 - \frac{2}{3}\left(\nabla\cdot\overline{\boldsymbol{v}}\right)^2\right) - \frac{2}{3}\omega\nabla\cdot\overline{\boldsymbol{v}}\right]$
    - $\alpha = 0.52$

A.4 LES

The filtered mass, momentum, and energy transport equations used in LES are

$$\frac{\partial}{\partial t} + \nabla\cdot\left(\rho\widetilde{\boldsymbol{v}}\right) = 0 \tag{A.21}$$

$$\frac{\partial}{\partial t}\left(\rho\widetilde{\boldsymbol{v}}\right) + \nabla\cdot\left(\rho\,\widetilde{\boldsymbol{v}}\bigotimes\widetilde{\boldsymbol{v}}\right) = -\nabla\cdot\widetilde{p}\boldsymbol{I} + \nabla\cdot\left(\widetilde{\boldsymbol{T}} + \boldsymbol{T}_{SGS}\right) + \boldsymbol{f}_b \tag{A.22}$$

$$\frac{\partial}{\partial t}\left(\rho\widetilde{E}\right) + \nabla\cdot\left(\rho\widetilde{E}\widetilde{\boldsymbol{v}}\right) = -\nabla\cdot\widetilde{p}\widetilde{\boldsymbol{v}} + \nabla\cdot\left(\widetilde{\boldsymbol{T}} + \boldsymbol{T}_{SGS}\right)\widetilde{\boldsymbol{v}} - \nabla\cdot\widetilde{\boldsymbol{q}} + \boldsymbol{f}_b\widetilde{\boldsymbol{v}} \tag{A.23}$$

where $\widetilde{\boldsymbol{v}}$ is the filtered velocity, $\widetilde{\boldsymbol{p}}$ is the filtered pressure, $\boldsymbol{I}$ is the identity tensor, f_b is the resultant body forces, $\widetilde{E}$ is the filtered total energy per unit mass, and $\widetilde{\boldsymbol{q}}$ is the filtered heat flux. The LES equations take the form of the RANS equations, except now the turbulent stress tensor represents the sub-grid scale stresses [34]. The subgrid scale stresses are modeled using the Boussinesq approximation

$$\boldsymbol{T}_{SGS} = 2\mu_t\boldsymbol{S} - \frac{2}{3}\left(\mu_t\nabla\cdot\widetilde{\boldsymbol{v}}\right)\boldsymbol{I} \tag{A.24}$$

where $\boldsymbol{S}$ is the strain rate tensor of the resolved velocity field $\overline{\boldsymbol{v}}$ (Equation 2.11).

A.4.1 WALE Subgrid Scale Model

In the WALE subgrid-scale model μ_t is taken to be

$$\mu_t = \rho \Delta^2 S_w \tag{A.25}$$

where Δ is the grid filter width and S_w is a deformation parameter. The grid filter width is calculated as

$$\Delta = min\left(\kappa d, C_w V^{1/3}\right) \tag{A.26}$$

where $C_w = 0.544$ and κ is the Von Karman constant which equals 0.41. The deformation paramter is defined as

$$S_w = \frac{S_d S_d^{3/2}}{S_d : S_d^{5/4} + S : S^{5/2}} \tag{A.27}$$

where

$$S_d = \frac{1}{2}\left[\nabla \boldsymbol{v} \cdot \nabla \boldsymbol{v} + (\nabla \boldsymbol{v} \cdot \nabla \boldsymbol{v})^T\right] - \frac{1}{3} tr\left(\nabla \boldsymbol{v} \cdot \nabla \boldsymbol{v}\right) \boldsymbol{I} \tag{A.28}$$